Research Square

Preprints are preliminary reports that have not undergone peer review.
They should not be considered conclusive, used to inform clinical practice,
or referenced by the media as validated information.

A Gallium-Doped Piezocatalytic Microsphere for Iron-Metabolism-Interfering Antibacterial Therapy and Repair of MRSA-Infected Bone Defects

Zhenghao Xie
Shandong Provincial Hospital
Tao Li
Shandong Provincial Hospital
Chao Sun
Shandong Provincial Hospital
Chuqi Zeng
Shandong First Medical University
Xingzhi Jing
Shandong Provincial Hospital
Cheng Liu
Shandong Provincial Hospital
Jiaju Ma
Shandong Provincial Hospital
Zhihao Xu
Shandong Provincial Hospital
Tianbao Ning
Shandong Provincial Hospital
Xiqiang Xu
Shandong Provincial Hospital
Ziliang Dong
Shandong First Medical University
Jun Dong
dongjun@sdfmu.edu.cn

Shandong Provincial Hospital

Research Article

Keywords: osteomyelitis, methicillin-resistant Staphylococcus aureus, piezocatalysis, iron metabolism, osteoclastogenesis

Posted Date: November 18th, 2026

DOI: https://doi.org/10.21203/rs.3.rs-11655553/v1

License: This work is licensed under a Creative Commons Attribution 4.0 International License.
Read Full License

Additional Declarations: No competing interests reported.

A Gallium-Doped Piezocatalytic Microsphere for Iron-Metabolism-Interfering Antibacterial Therapy and Repair of MRSA-Infected Bone Defects

Zhenghao Xie[1,†], Tao Li[1,†], Chao Sun[1,†], Chuqi Zeng[2,†], Xingzhi Jing[1], Cheng Liu[1], Jiaju Ma[1], Zhihao Xu[1], Tianbao Ning[1], **Xiqiang Xu**[1,*], **Ziliang Dong**[2,*], **Jun Dong**[1,*]

1 Department of Spine Surgery, Shandong Provincial Hospital Affiliated to Shandong First Medical University, Jinan, Shandong, 250021, P. R. China

2 Science and Technology Innovation Center, Shandong First Medical University & Shandong Academy of Medical Sciences, Jinan, Shandong, 250117, P. R. China

Correspondence to: Xiqiang Xu (xuxiqiang@email.sdfmu.edu.cn), Ziliang Dong (dongziliang@sdfmu.edu.cn) or Jun Dong (dongjun@sdfmu.edu.cn).

† These authors contributed equally: Zhenghao Xie, Tao Li, Chao Sun and Chuqi Zeng.

Abstract

Background: Bacterial bone infections, particularly those caused by methicillin-resistant Staphylococcus aureus (MRSA), create a hostile microenvironment in which persistent pathogens, biofilm barriers, inflammatory osteolysis, and impaired bone repair coexist, making osteomyelitis notoriously refractory to conventional antibiotics.

Results: Here, we engineer Ga-doped bismuth oxychloride (BiOCl-Ga) piezocatalytic nanosheets encapsulated within porous poly(lactic-co-glycolic acid) (PLGA) microspheres (denoted as GaBi@MS), for ultrasound (US)-triggered piezocatalysis, and Ga-mediated interference with iron-dependent bacterial metabolism. Ga incorporation narrows the band gap and enhances piezocatalytic performance. Under US irradiation, GaBi@MS causes severe MRSA membrane damage, lipid peroxidation, and biofilm disruption. Meanwhile, owing to the chemical mimicry between Ga and Fe, Ga ions compete with and replace Fe within bacteria, disrupting bacterial iron metabolism and thereby killing the pathogens. In osteoclast models, GaBi@MS+US can suppress MRSA-induced osteoclastogenesis, reducing labile iron, TFR1/c-Fos/NFATC1/TRAP signaling, TRAP-positive osteoclasts, and F-actin-ring formation. Meanwhile, in both osteomyelitis and infected calvarial-defect models, GaBi@MS effectively kills bacteria through US-triggered piezocatalysis and Ga-mediated iron metabolism interference, while alleviating inflammation, osteoclast activity, and osteolysis, thereby preserving bone architecture and promoting repair.

Conclusions: Collectively, this platform couples remotely triggered oxidative antibacterial activity with iron-sensitive regulation of the pathogen-osteoclast axis while preserving the osteoblast compartment.

Keywords: osteomyelitis; methicillin-resistant Staphylococcus aureus; piezocatalysis; iron metabolism; osteoclastogenesis

Background

Acute suppurative osteomyelitis is a destructive infection of bone and bone marrow that remains a major challenge in orthopedic practice. Persistent bacterial colonization, biofilm formation, inflammatory-cell infiltration, and progressive osteolysis can culminate in delayed healing, structural instability, pathological fracture, and long-term functional impairment [1, 2]. MRSA is particularly difficult to eradicate because antimicrobial resistance, biofilm-associated protection, and persistence within host tissues collectively reduce treatment efficacy [2, 3, 4]. Systemic antibiotics and surgical debridement remain indispensable, yet poor drug penetration into infected bone and mature biofilms, residual bacterial reservoirs, and recurrent infection can necessitate prolonged therapy or repeated

procedures [1, 3, 4, 5]. Local antibiotic carriers, including polymeric and cement-based systems, can increase lesion-site exposure [6, 7, 8, 9, 10], but they primarily address bacterial burden and do not directly restrain the pathological bone resorption that continues to compromise skeletal integrity [8, 11]. A clinically meaningful local strategy should therefore combine infection control with suppression of infection-associated osteoclast activity and osteolysis while preserving osteoblast-lineage competence.

Iron metabolism provides a mechanistic bridge between bacterial persistence and pathological bone resorption. *S. aureus* requires iron for respiration, DNA synthesis, central-carbon metabolism, redox homeostasis, and virulence, and therefore relies on tightly regulated siderophore- and heme-acquisition systems within the iron-restricted host environment [12, 13, 14, 15, 16]. Osteoclasts are likewise iron dependent: differentiation and resorptive maturation require mitochondrial bioenergetics, redox signaling, cytoskeletal remodeling, and transferrin-receptor-mediated iron uptake [17, 18, 19]. Excess iron can amplify oxidative/NF-κB-associated osteoclastogenesis [17], whereas *S. aureus* itself promotes osteoclast formation through inflammatory and NF-κB-dependent signaling [20]. Thus, iron handling represents a shared biological vulnerability linking persistent MRSA infection to the host resorptive program that drives infection-associated bone loss.

Gallium offers a distinctive means of exploiting this shared iron dependence. Ga^{3+} resembles Fe^{3+} in ionic radius and coordination chemistry and can enter iron-associated uptake and binding pathways, yet it cannot sustain physiological Fe^{2+}/Fe^{3+} redox cycling [12, 13, 16, 21, 22]. This redox inactivity disrupts multiple iron- and heme-dependent bacterial processes and underlies the antimicrobial activity of Ga-based agents [12, 13, 21, 22]. Accordingly, Ga-containing materials have been explored to interfere with bacterial iron metabolism for infection treatment. Recent studies have shown that Ga-based systems can perturb iron acquisition and utilization, biofilm formation, and quorum sensing [23], while Ga-doped polydopamine coatings on titanium combine Ga-mediated iron interference with photothermal antibacterial activity and favorable osteogenic responses [24]. Together with the broad targeting of iron/heme-dependent biological processes by Ga(III) compounds [13], these findings

support Ga-based iron interference as a promising antibacterial strategy for bone infections requiring both bacterial clearance and tissue repair.

In this study, we designed Ga-doped piezocatalytic microspheres that integrate ultrasound-triggered piezocatalysis with Ga-mediated iron metabolism interference. Ga doping narrows the band gap and enhances the piezocatalytic performance of the system, enabling efficient generation of reactive oxygen species under ultrasound irradiation. Meanwhile, the gallium-containing component may interfere with iron-associated bacterial processes, potentially disturbing iron homeostasis and heme-dependent functions. This dual mechanism, piezocatalytic oxidative attack combined with iron-metabolism interference, enables synergistic antibacterial action while simultaneously suppressing pathological osteoclastogenesis. In both osteomyelitis and infected calvarial-defect models, GaBi@MS+US effectively killed bacteria and alleviated inflammation, osteoclast activity, and osteolysis, thereby preserving bone architecture and promoting repair. Collectively, this design couples piezocatalytic antibacterial therapy with Ga-based iron interference, aiming to eradicate MRSA while preserving osteogenic capacity.

Methods

Preparation of Ga-doped BiOCl nanosheets and microspheres

Ga doped BiOCl nanosheets were prepared by a solvothermal method. Briefly, 552.9 mg of bismuth nitrate pentahydrate ($Bi(NO_3)_3 \cdot 5H_2O$) was dissolved in 36 mL of ethylene glycol under magnetic stirring to form a homogeneous solution. Meanwhile, 70.2 mg of sodium chloride (NaCl) and 240 mg of polyvinylpyrrolidone (PVP) were separately dissolved in 3 mL of ultrapure water. Subsequently, the NaCl and PVP solutions were added dropwise to the above bismuth nitrate ethylene glycol solution under continuous stirring. After thorough mixing, 10.56 μL of anhydrous gallium chloride ($GaCl_3$) was introduced, and the mixture was bath-sonicated to ensure uniform dispersion, yielding a homogeneous reaction solution. The resulting mixture was transferred to a Teflon-lined stainless-steel autoclave and subjected to solvothermal reaction at 120 °C for 8 h. After the reaction, the autoclave was allowed to cool naturally to room temperature. The product was collected and washed thoroughly with anhydrous

ethanol to remove unreacted precursors and byproducts. Finally, the resulting BiOCl-Ga nanosheets were then used for subsequent experiments.

GaBi@MS were prepared by a double-emulsion solvent evaporation method. Briefly, 10 mg of BiOCl-Ga and 12.5 mg of NH_4HCO_3 were dispersed in 0.625 mL of ultrapure water, while 38 mg of PLGA was dissolved in 2 mL of dichloromethane (DCM). The aqueous dispersion was mixed with the PLGA solution and emulsified by probe sonication to form a homogeneous emulsion. The emulsion was then injected into 50 mL of 1% (w/v) PVA solution and stirred overnight at room temperature to evaporate DCM. The microspheres were collected by sedimentation, washed three times with ultrapure water, and lyophilized. During lyophilization, the encapsulated NH_4HCO_3 decomposed to release CO_2 and NH_3, generating a porous structure within the PLGA matrix. The resulting GaBi@MS was stored at 4 °C for further use.

Characterization and piezocatalytic performance of GaBi@MS

The morphology of GaBi nanosheets was observed by TEM (Talos 200X, Sigma), and elemental distribution was analyzed by HAADF-STEM elemental mapping. XPS survey spectra (Thermo Fisher Scientific K-Alpha) were recorded to confirm the elemental composition and Ga incorporation. DLS (Malvern Zetasizer Pro) was used to measure the particle size and zeta potential of BiOCl and GaBi. UV-vis DRS was performed to determine the band gap. PFM (Bruker Dimension ICON) characterization was carried out to evaluate the piezoelectric properties of GaBi, including phase hysteresis loops and amplitude-voltage curves over a bias range of -10 to +10 V. The morphology and porous structure of the microspheres were observed by SEM (Zeiss Sigma 300), and EDS mapping was used to confirm the distribution of Bi, O, Cl, Ga, and C. TGA was performed to analyze the thermal decomposition behavior of the microspheres (PerkinElmer TGA 8000). The piezoelectric current, potential, and electrochemical impedance spectroscopy (EIS) were measured using an electrochemical workstation (Shanghai Chenhua).

Piezoelectric and electrochemical measurements

The piezoelectric current and potential responses of GaBi@MS, BiOCl@MS, and blank groups were recorded under cyclic ultrasound on/off irradiation (30 kHz, 4.0 W cm^{-2}) using an electrochemical

workstation. EIS was further conducted to analyze interfacial charge transfer resistance before and after US irradiation, with Nyquist plots recorded to assess the effect of the US-induced piezoelectric effect on electron transfer.

Detection of ROS generation

The ·OH generation capacity of GaBi@MS under US stimulation was evaluated using MB as a probe. Specifically, 7.5 μL of MB (1.5 mg mL^{-1}) was introduced into 1 mL of deionized water containing GaBi@MS (90 μg mL^{-1}). Following US exposure (30 kHz, 4.0 W cm^{-2}) for varying durations, the absorbance of MB at 662 nm was recorded on a UV-Vis-NIR spectrophotometer. A progressive decline in MB absorbance was taken as evidence of ·OH production.

The $^1O_2$ generation capacity was assessed using DPBF as a probe. In brief, 20 μL of DPBF (1 mg mL^{-1}) was added to 1 mL of GaBi@MS suspension (90 μg mL^{-1}), and the mixture was subjected to US exposure (30 kHz, 4.0 W cm^{-2}) for different time intervals. The absorbance of DPBF at 416 nm was then monitored by UV-Vis-NIR spectrophotometry. A time-dependent decrease in DPBF absorbance indicated the generation of $^1O_2$.

The corresponding supplementary characterization data, including high-resolution XPS spectra, XRD patterns, zeta-potential measurements, TGA curves, and EIS Nyquist plots, are presented in Figures S1–S5.

In vitro antibacterial and antibiofilm assays

MRSA (CCTCC AB 2010021) was cultured in Luria-Bertani (LB) broth at 37 °C. A single colony from a fresh LB agar plate was cultured overnight with shaking, washed twice with sterile PBS, and adjusted to 1×10^8 CFU/mL. Unless otherwise specified, groups were CON, MS, GaBi@MS, BiOCl@MS+US, and GaBi@MS+US; microspheres were used at 100 μg/mL, and US was applied at a frequency of 30 kHz and an intensity of 4.0 W cm^{-2} once for 15 min under the conditions described above. In the MS group, blank PLGA microspheres received the same US exposure as the US-treated groups, whereas GaBi@MS was not exposed to US.

For colony-recovery assays, separate bacterial cultures were prepared for each group and endpoint. The assigned microspheres were added at the beginning of culture, the designated groups received a single US treatment, and samples were collected on days 1, 3, and 7. Each sample was serially diluted in sterile PBS and plated on LB agar for viable-colony enumeration. For membrane-integrity analysis, treated bacteria were washed and stained with SYTO 9/PI according to the manufacturer's protocol (LABLEAD), and at least five random microscopic fields were recorded per sample. For biofilm assays, MRSA was statically cultured for 72 h with daily medium replacement, treated according to group assignment, fixed with 4% paraformaldehyde, stained with 0.1% crystal violet, and quantified as residual biofilm biomass at OD570.

For membrane-associated flow cytometry, treated bacteria were incubated with Annexin V-FITC/PI for 15 min in the dark and analyzed using a CytoFLEX flow cytometer (Beckman Coulter; ≥10,000 events/sample); populations were reported by staining status without assigning eukaryotic apoptotic categories. For ultrastructural analysis, bacteria were fixed in 2.5% glutaraldehyde. SEM samples were dehydrated, critical-point dried, sputter-coated, and imaged using a Nova Nano 450 microscope at 5 kV; TEM samples were post-fixed with 1% osmium tetroxide, resin-embedded, sectioned at 70–90 nm, stained with uranyl acetate/lead citrate, and examined using an HT7800 microscope at 80 kV.

For supplementary quantitative analyses, residual crystal-violet biofilm biomass was quantified at OD570, SYTO 9/PI images were quantified as relative bacterial survival, Annexin V-FITC/PI flow-cytometric data were quantified as the percentage of positive bacterial events, and viable colony recovery was expressed as CFU/mL on days 1, 3, and 7 (Figures S6–S9).

Antibacterial mechanism and untargeted metabolomics

After treatment, bacterial suspensions were collected and washed with PBS. Intracellular oxidant-associated fluorescence was measured by incubating bacteria with 2′,7′-dichlorodihydrofluorescein diacetate (DCFH-DA), followed by fluorescence microscopy and flow cytometry (≥10,000 singlet events) [35]. Lipid peroxidation was evaluated using a fluorescent lipid-peroxidation probe according to the manufacturer's instructions. For the labile Fe^{2+}-associated pool, treated bacteria were incubated with FerroOrange, washed, and imaged under identical acquisition settings [36]. Aconitase activity

and intracellular ATP content were measured from treated bacterial lysates using commercial kits (Solarbio, Beijing, China) according to the manufacturer's protocols.

For the supplementary quantitative readouts, C11-BODIPY lipid peroxidation was expressed as the oxidized/reduced fluorescence ratio, DCFH-DA fluorescence was normalized to the CON group, and FerroOrange fluorescence was quantified as relative fluorescence intensity (Figures S10–S12).

For untargeted metabolomics, three independent biological replicates from each of the CON and GaBi@MS+US groups were extracted with pre-cooled methanol and analyzed using a Vanquish UHPLC system coupled to a Q Exactive high-resolution mass spectrometer with an ACQUITY UPLC HSS T3 column. Raw data were processed using Compound Discoverer 3.3 and annotated against mzCloud, mzVault, and ChemSpider. Principal component analysis (PCA) and orthogonal partial least-squares discriminant analysis (OPLS-DA) were performed in R 4.3.1. Differential metabolites were defined by VIP > 1 and $P < 0.05$ and subjected to hierarchical clustering, functional classification, and KEGG enrichment analysis.

MC3T3-E1 cytocompatibility and osteogenic assays

MC3T3-E1 pre-osteoblasts were cultured in minimum essential medium supplemented with 10% FBS and 1% penicillin-streptomycin at 37 °C and 5% CO_2.

For CCK-8 assays, cells were seeded at 5×10^3 cells/well. Concentration-dependent cytocompatibility was evaluated after 24 h exposure to GaBi@MS at 25, 50, 100, 250, 500, and 1000 μg/mL. Time-dependent experiments comprised CON, MS, GaBi@MS, BiOCl@MS+US, and GaBi@MS+US groups at 100 μg/mL and were evaluated on days 1, 3, and 7.

Except for the infection-challenge experiment, osteoblast assays were performed under bacteria-free conditions. F-actin organization and Runx2 expression were assessed by Actin-Tracker Red-555/DAPI staining and Runx2 immunofluorescence, respectively; OPN and Runx2 were analyzed by western blotting. Under osteogenic induction, ALP staining was performed on day 7 and Alizarin Red S staining on day 14. These experiments were designed to test cytocompatibility and preservation of osteogenic competence, not to establish direct osteoinduction.

Runx2 and OPN western-blot bands were quantified by densitometry and normalized to GAPDH for the supplementary analyses.

For infection-associated survival, cells were assigned to CON, Infection (MRSA), and MRSA + GaBi@MS+US. The latter two groups were challenged overnight with MRSA (1×10^8 CFU/mL), and the treatment group additionally received GaBi@MS+US. Cell survival was evaluated by Calcein-AM/PI staining and image-based viability quantification.

Osteoclast, iron-loading and RNA-sequencing assays

RAW264.7 cells were maintained in high-glucose DMEM supplemented with 10% FBS and 1% penicillin-streptomycin at 37 °C and 5% CO_2. Osteoclast differentiation was induced with macrophage colony-stimulating factor (M-CSF; 30 ng/mL) and receptor activator of nuclear factor-κB ligand (RANKL; 50 ng/mL) for 5–6 days, with medium renewal every 2 days.

For the baseline osteoclast and transcriptomic experiments, groups were Ctrl (M-CSF alone), RANKL (M-CSF + RANKL), and Ga (M-CSF + RANKL + GaBi@MS+US). Accordingly, 'Ga' in the RNA-seq analyses denotes the RANKL + GaBi@MS+US condition and should not be interpreted as a FAC-treated group.

For infection-associated osteoclastogenesis, RANKL-induced cultures were assigned to RANKL, RANKL + MRSA, or RANKL + MRSA + GaBi@MS+US. The latter two groups were challenged overnight with MRSA (1×10^8 CFU/mL). Osteoclast-like cells were evaluated by tartrate-resistant acid phosphatase (TRAP) staining, and TRAP-positive area was quantified from non-overlapping fields acquired under identical settings.

For iron-loading experiments, RANKL-induced cells were assigned to CON, ferric ammonium citrate (FAC), FAC + Ga, and FAC + deferoxamine (DFO). FAC was applied at 100 μM for 24 h, the Ga intervention consisted of GaBi@MS at 100 μg/mL followed by the US regimen described above, and DFO was applied at 100 μmol/L. Here, “Ga” is used only as a shorthand for GaBi@MS+US; therefore, FAC + Ga denotes FAC-treated cells receiving GaBi@MS+US rather than free Ga ions or a Ga-only treatment. Intracellular Fe^{2+} was quantified by a ferrozine-based colorimetric assay at 562 nm and normalized to total protein measured with a bicinchoninic acid (BCA) assay (OD568), yielding

nmol Fe^{2+} per mg protein. FerroOrange imaging provided an independent fluorescence-based readout of the labile Fe^{2+}-associated pool. TFR1 abundance was additionally assessed by immunofluorescence using an anti-TFR1 primary antibody (Abcam) with DAPI nuclear counterstaining; images were acquired under identical settings and relative fluorescence intensity was quantified using ImageJ. Osteoclast maturation was assessed by whole-well TRAP staining and Actin-Tracker/DAPI visualization of peripheral F-actin rings. Mitochondrial membrane-potential profiles were measured by JC-1 flow cytometry using a CytoFLEX instrument. NFATC1, TFR1, c-Fos, TRAP, and GAPDH were analyzed by western blotting and densitometry.

For supplementary quantification of the iron-loading experiments, TRAP-positive area was measured as the percentage of the analyzed field. Intracellular oxidant-associated DCF fluorescence in osteoclasts was additionally assessed by flow cytometry and summarized as relative median DCF fluorescence intensity (Figure S14A, B).

For RNA sequencing, three independent biological replicates from each Ctrl, RANKL, and Ga group underwent poly(A)-enriched library preparation followed by 150-bp paired-end sequencing on the DNBSEQ-T7 platform. Reads were processed with fastp, HISAT2, and StringTie, and differential expression was analyzed with DESeq2 for RANKL versus Ctrl and Ga versus RANKL ($|\log_2 FC| \geq 1$, $P < 0.05$). GO/KEGG enrichment, hierarchical clustering, selected-gene analyses, and GSEA were used to interrogate osteoclast differentiation, iron uptake/storage, mitochondrial iron handling, heme/redox metabolism, phagolysosomal and autophagic programs, HIF-1 signaling, mineral absorption, and ferroptosis-related gene sets. FAC-treated cells were not independently sequenced.

Animal models and treatment

Animal experiments were conducted at the Laboratory Animal Center of Shandong Provincial Hospital Affiliated to Shandong First Medical University under SPF conditions and were approved by the Institutional Animal Care and Use Committee of Shandong First Medical University (Approval No. 2025-073). Eight-week-old male C57BL/6 mice were randomized to PBS, MRSA, vancomycin, or GaBi@MS+US (n = 5/group). PBS served as the uninfected surgical control; all other groups received the same MRSA inoculum.

For femoral osteomyelitis, a 0.5-mm cortical defect was created in the right femur under intraperitoneal Avertin anesthesia (tribromoethanol, 250 mg/kg), following established experimental osteomyelitis principles [37]. PBS mice received 10 μL sterile PBS, whereas the MRSA, vancomycin, and GaBi@MS+US groups received 10 μL MRSA (1×10^8 CFU/mL) into the cortical defect/medullary region. Vancomycin was administered intravenously at 50 mg/kg every 12 h for 7 days. GaBi@MS+US mice received local GaBi@MS (5 mg/kg) on days 0, 3, and 6, each followed by 15 min of transcutaneous US. Femora were harvested on day 21.

For the MRSA-inoculated calvarial-defect model, a 2.5-mm full-thickness defect was created in the left parietal bone. PBS mice received a gelatin sponge loaded with sterile PBS; MRSA and vancomycin mice received sponges loaded with 10 μL MRSA (1×10^8 CFU/mL); and GaBi@MS+US mice received a single sponge co-loaded with the same MRSA inoculum and GaBi@MS (5 mg/kg). The material-containing sponge was implanted once and was not replaced. US was applied transcutaneously for 15 min on days 0, 3, and 6, and vancomycin followed the femoral regimen. Calvaria were harvested at week 8.

At predefined endpoints, mice were euthanized by gradual-fill CO_2 inhalation followed by cervical dislocation as a secondary method.

In vivo imaging, micro-CT, and histology

To assess the local retention and degradation/clearance trend of the microsphere carrier, Cy5-labeled PLGA microspheres were longitudinally imaged at the femoral site on days 1, 3, 5, 7, 14, and 21 using a small-animal fluorescence-imaging system (excitation, 637 nm; emission, 672 nm; 655–690 nm band-pass filter). Identical regions of interest were applied after background subtraction, and Cy5-associated radiant efficiency was quantified using the same acquisition settings; this signal was used to track the labeled carrier rather than bacterial burden.

For the supplementary longitudinal analysis, Cy5-labeled PLGA carrier-associated fluorescence was expressed as average radiant efficiency, with individual trajectories retained for the five imaged mice (Figure S13).

Fixed femora and calvaria were scanned using a nanoVoxel-3000 micro-CT system. Femoral regions centered on the cortical defect were analyzed for BV/TV, Tb.N, Tb.Th, and Tb.Sp; the calvarial region of interest encompassed the entire 2.5-mm defect. Identical acquisition, reconstruction, and segmentation settings were used within each model.

After micro-CT, specimens were decalcified in 10% EDTA for 4 weeks, paraffin-embedded, and sectioned at 1 μm. Femora were evaluated by H&E and TRAP staining, and calvaria by H&E and Masson's trichrome staining. Femoral sections were additionally immunostained for TNF-α, IL-6, OCN, RANKL, and GPX4. Histological and immunohistochemical signals were quantified using ImageJ under identical image-acquisition settings.

Statistical analysis

Unless otherwise specified, cell-based experiments included three independent biological replicates, bacterial in vitro experiments included at least three independent biological replicates, and animal experiments included five biologically independent mice per group. Technical replicates were averaged before statistical analysis. Data are presented as mean ± SD. Statistical analyses were performed using GraphPad Prism 11, and image quantification was performed using ImageJ.

Two-group comparisons used two-tailed unpaired Student's t-tests. Multiple groups were compared by one-way ANOVA with Tukey's post hoc test, whereas time- or concentration-dependent datasets were analyzed by two-way ANOVA with appropriate multiple-comparison correction. Longitudinal fluorescence data were analyzed by repeated-measures ANOVA or mixed-effects modeling when values were missing. A two-sided $P < 0.05$ was considered statistically significant. Animals were randomized, and micro-CT reconstruction and histological analyses were performed blinded to group allocation.

Results

Preparation and characterization of gallium-doped piezocatalytic porous microspheres

First, the Ga-doped Piezocatalytic porous microspheres (GaBi@MS) were prepared by a double-emulsion solvent evaporation method, in which Ga-doped BiOCl nanosheets were first synthesized by

a solvothermal method (Fig. 1A). Transmission Electron Microscopy (TEM) revealed an irregular sheet-like morphology with a lateral size of approximately 90.3 nm (Fig. 1B). High-Angle Annular Dark-Field Scanning TEM (HAADF-STEM) elemental mapping showed uniform distribution of Bi, O, Cl, and Ga within the nanosheets, and X-ray Photoelectron Spectroscopy (XPS) survey spectra further confirmed the coexistence of Ga 2p and Bi, O, Cl, indicating successful Ga incorporation (Fig. 1C, D; Figure S1). X-ray diffraction (XRD) patterns showed that Ga doping did not alter the host crystal phase of BiOCl, with all diffraction peaks matching well with the standard card of BiOCl (PDF#06-0249) (Figure S2). DLS showed a slight increase in particle size after Ga doping, and the zeta potential changed from -20.4 mV for BiOCl to -16.4 mV for Ga doped BiOCl (GaBi) (Fig. 1E; Figure S3). UV-vis Diffuse Reflectance Spectroscopy (DRS) indicated that the band gap was decreased from 3.58 eV for BiOCl to 3.46 eV for GaBi (Fig. 1F). Piezoresponse force microscopy (PFM) characterization confirmed the piezoelectric nature of GaBi, evidenced by a well-defined phase hysteresis loop together with a butterfly-shaped amplitude–voltage curve acquired over a bias range of -10 to +10 V (Fig. 1G). Subsequently, GaBi was loaded into PLGA microspheres. Scanning Electron Microscopy (SEM) showed regularly spherical microspheres with porous surfaces, and EDS mapping confirmed uniform distribution of Bi, O, Cl, Ga, and C within the microspheres (Fig. 1H). Thermogravimetric analysis (TGA) revealed decomposition of the PLGA matrix and inorganic residues (Figure S4). Then, FITC and Cy5 were used to label GaBi and PLGA, respectively. Confocal imaging at different depths (2, 5, 10, and 16 μm) displayed clear fluorescence, demonstrating an interconnected porous structure within the microspheres and uniform distribution of both components (Fig. 1I). Under US irradiation, the piezoelectric current and potential responses of GaBi@MS were higher than those of BiOCl@MS and the blank group, exhibiting stable and reversible on/off behavior, indicating that Ga doping improved charge separation efficiency (Fig. 1J, K). Meanwhile, Electrochemical Impedance Spectroscopy analysis showed that the Nyquist semicircle radius of GaBi@MS after US irradiation was smaller than that of the non-irradiated group, indicating that the US-induced piezoelectric effect reduced interfacial charge transfer resistance and accelerated electron transfer (Figure S5). Finally, 3,3′,5,5′-Tetramethylbenzidine (TMB) and 1,3-Diphenylisobenzofuran (DPBF) probes confirmed the generation of hydroxyl radicals and singlet oxygen under US conditions,

with TMB absorbance increasing and DPBF absorbance decreasing with prolonged irradiation (Fig. 1L–N). In summary, our GaBi@MS exhibited a porous structure, excellent piezoelectric performance, and efficient piezocatalytic ROS generation under US stimulation (Fig. 1O).

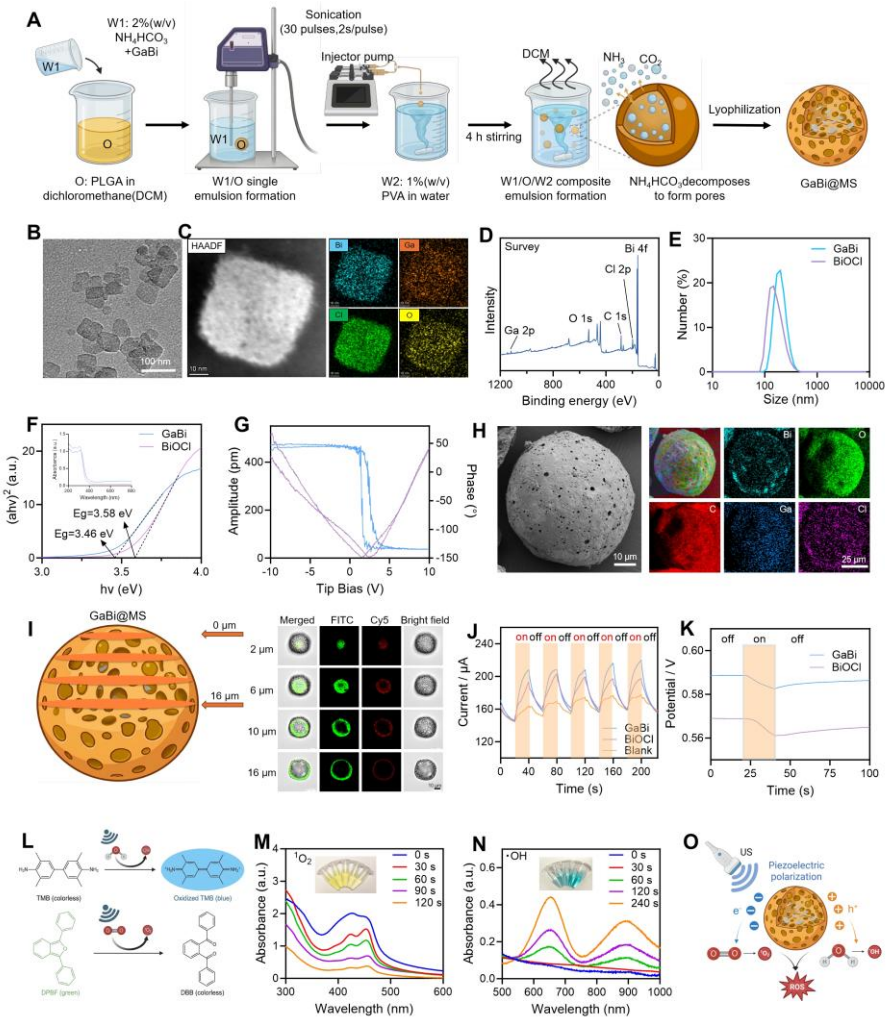


Fig. 1. Preparation and characterization of gallium-doped piezocatalytic porous microspheres. A Schematic illustration of the preparation of GaBi@MS by a double-emulsion solvent evaporation method. B TEM image of GaBi nanosheets. C HAADF-STEM elemental mapping of Bi, O, Cl, and Ga in GaBi nanosheets. D XPS survey spectrum of GaBi. E DLS size distribution and zeta potential of BiOCl and GaBi. F UV-vis DRS and the corresponding band gaps of BiOCl and GaBi. G PFM phase hysteresis loop and amplitude-voltage curve of GaBi. H SEM image and EDS mapping of GaBi@MS. I Confocal fluorescence images of GaBi@MS at different depths. J, K Piezoelectric current and potential responses of GaBi@MS, BiOCl@MS, and blank groups under cyclic US on/off irradiation. L – N Detection of ROS generation by GaBi@MS using TMB and DPBF probes under US irradiation. O Schematic illustration of the piezoelectric effect promoting ROS generation by GaBi@MS upon US stimulation.

US-activated GaBi@MS damages MRSA envelopes and suppresses biofilms and bacterial recovery

We next evaluated the antibacterial performance of the platform against MRSA using complementary biofilm, colony-recovery, membrane-integrity, and ultrastructural assays. Crystal-violet staining showed dense biofilm biomass in the CON and MS groups, indicating that blank PLGA microspheres with US did not appreciably disrupt the established biofilm phenotype. GaBi@MS without US produced a modest reduction in residual staining, whereas the US-activated BiOCl@MS and GaBi@MS groups showed substantially less crystal-violet retention. The weakest residual staining was observed in the GaBi@MS+US group, consistent with the strongest suppression of mature biofilm biomass under the combined treatment condition (Fig. 2A; Figure S6).

Membrane-integrity staining showed the same treatment-dependent pattern. SYTO 9/PI imaging was dominated by green fluorescence in CON and MS, whereas GaBi@MS alone increased the fraction of PI-positive bacteria and US-activated treatment caused a pronounced shift toward red fluorescence, with the greatest membrane-compromised signal in GaBi@MS+US (Fig. 2C; Figure S7). Annexin V-FITC/PI flow cytometry independently showed redistribution of bacterial events toward staining-positive populations after active treatment, again most prominently after GaBi@MS+US (Fig. 2E; Figure S8). These flow-cytometric populations were interpreted according to staining status rather than eukaryotic apoptotic categories.

The colony-recovery experiment further assessed whether a single material administration and US exposure produced only an immediate antibacterial effect or also limited subsequent bacterial regrowth. At days 1, 3, and 7, CON and MS plates remained densely populated, whereas GaBi@MS alone reduced the recoverable bacterial burden to a lesser extent. US activation of BiOCl@MS markedly decreased colony formation, and GaBi@MS+US consistently yielded the fewest colonies across all three time points (Fig. 2B; Figure S9). The persistence of this hierarchy through day 7 indicates that the combined treatment did not merely transiently inhibit plating efficiency but produced sustained suppression of viable bacterial recovery under the conditions tested.

Direct imaging of bacterial morphology provided structural confirmation of the membrane assays. SEM showed relatively smooth and intact coccoid surfaces in CON and MS, while treated bacteria developed progressively greater surface corrugation, collapse, and discontinuity. TEM further revealed loss of normal envelope definition, cytoplasmic rarefaction, membrane separation, and leakage-like ultrastructural changes, with the most extensive destruction in the GaBi@MS+US group (Fig. 2D). Thus, biofilm reduction, persistent loss of colony recovery, membrane-permeability changes, and direct ultrastructural injury converged on the same treatment hierarchy. The experimentally supported antibacterial sequence is summarized in Fig. 2F: US-activated piezocatalytic oxidative injury acts on the bacterial envelope and intracellular redox state, while the Ga-containing component provides an additional iron/metabolic constraint.

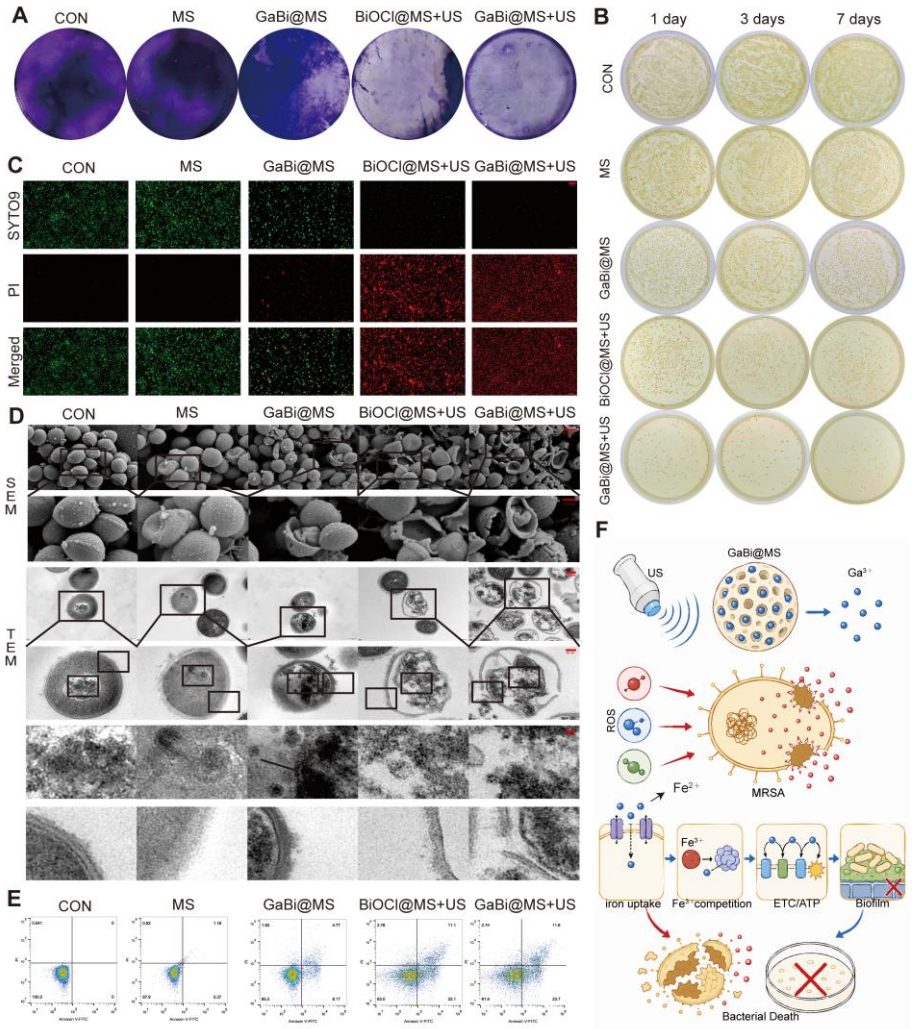


Fig. 2. US-activated GaBi@MS damages MRSA envelopes and suppresses biofilms and bacterial recovery. A Crystal-violet staining of established MRSA biofilms after the indicated treatments. **B** Representative agar-plate colony recovery on days 1, 3 and 7 after one material administration and the indicated US exposure. **C** SYTO 9/propidium iodide (PI) fluorescence images showing bacterial membrane integrity. **D** Scanning and transmission electron microscopy images of bacterial morphology and envelope ultrastructure. **E** Annexin V–FITC/PI flow-cytometry profiles, interpreted as staining-defined populations rather than eukaryotic apoptotic categories. **F** Proposed summary of US-associated oxidative injury and gallium-associated iron/metabolic stress, based on the experiments shown. MRSA, methicillin-resistant Staphylococcus aureus; US, ultrasound; CON, untreated MRSA; MS, blank poly(lactic-co-glycolic acid) microspheres with US; GaBi@MS, gallium-doped BiOCl-loaded microspheres without US; BiOCl@MS+US, BiOCl-loaded microspheres with US; GaBi@MS+US, gallium-doped BiOCl-loaded microspheres with US. Representative images were obtained in at least three independent experiments.

Ultrasound-activated GaBi@MS couples oxidative injury with metabolic remodeling in MRSA

First, we explored the potential of GaBi@MS under ultrasound-activated piezoelectric stimulation to induce oxidative stress in MRSA. The lipid-peroxidation probe showed a marked treatment-dependent shift after exposure to the active materials: CON and MS retained the baseline fluorescence pattern, whereas US-activated groups displayed a strong oxidation-associated signal, with GaBi@MS+US showing the most pronounced change (Fig. 3A; Figure S10). DCFH-DA microscopy similarly showed little oxidant-associated fluorescence in CON and MS, a moderate increase with GaBi@MS alone, and a strong increase after US activation, particularly in the GaBi@MS+US group (Fig. 3B).

We then assessed two metabolic readouts linked to central energy and iron-dependent enzymatic processes. The aconitase assay produced a linear standard curve, and intracellular aconitase activity differed markedly among groups (Fig. 3C). Activity was lower in MS than in CON, increased in the GaBi@MS and BiOCl@MS+US groups, and reached the highest measured level after GaBi@MS+US treatment. ATP quantification showed a similar overall increase across the active-treatment groups, with the greatest ATP content in GaBi@MS+US (Fig. 3D). Importantly, these increases occurred in the same samples in which colony recovery, membrane integrity, and ultrastructure were severely impaired. Accordingly, the elevated aconitase and ATP readouts were interpreted as part of a dysregulated or compensatory metabolic response to severe treatment stress rather than evidence of improved bacterial fitness.

Flow-cytometric DCF measurements showed a treatment-associated redistribution of oxidant-associated fluorescence at the population level (Fig. 3E; Figure S11). Because Ga can enter iron-associated biological pathways, we next examined the labile Fe^{2+}-associated pool using FerroOrange. In contrast to the oxidative probes, FerroOrange fluorescence was reduced in the Ga-containing conditions and reached its lowest level after GaBi@MS+US treatment (Fig. 3F; Figure S12). This reciprocal pattern, enhanced oxidant/lipid-peroxidation signals together with a diminished labile iron-associated fluorescence, supports simultaneous redox injury and disturbance of intracellular iron handling rather than oxidative damage alone.

Untargeted metabolomics was therefore used to place these biochemical observations into a broader metabolic context. Comparison of CON and GaBi@MS+US identified 1264 differential metabolic features, including 454 increased and 810 decreased signals (Fig. 3G). After annotation and filtering, 237 metabolites were retained for pathway-oriented interpretation, of which 124 were increased and 113 decreased. Representative differential metabolites mapped to amino-acid stress, nucleotide/energy metabolism, iron/heme-associated processes, membrane metabolism, and ROS/redox pathways (Fig. 3H). KEGG analysis further highlighted pathways related to quorum sensing, ABC transporters, two-component signaling, nucleotide and purine/pyrimidine metabolism, carbon metabolism, cysteine/methionine metabolism, glyoxylate/dicarboxylate metabolism, and the TCA cycle (Fig. 3I). Functional grouping of the differential metabolites showed that the response was distributed across nucleotide/purine metabolism, amino-acid stress, ROS/redox homeostasis, lipid/membrane metabolism, electron-transport cofactors, energy/TCA metabolism, biofilm/cell-wall-associated processes, and iron/heme metabolism (Fig. 3J). The hierarchical heatmap separated CON and GaBi@MS+US replicates and showed coordinated changes across these functional categories rather than isolated movement of a single metabolite (Fig. 3K). Together with the membrane and biofilm phenotypes described above, these data indicate that GaBi@MS+US imposes a multi-layered antibacterial stress characterized by piezocatalytic oxidative injury, membrane lipid damage, disruption of the bacterial labile-iron-associated pool, and broad metabolic remodeling involving energy, nucleotide, redox, and iron/heme networks.

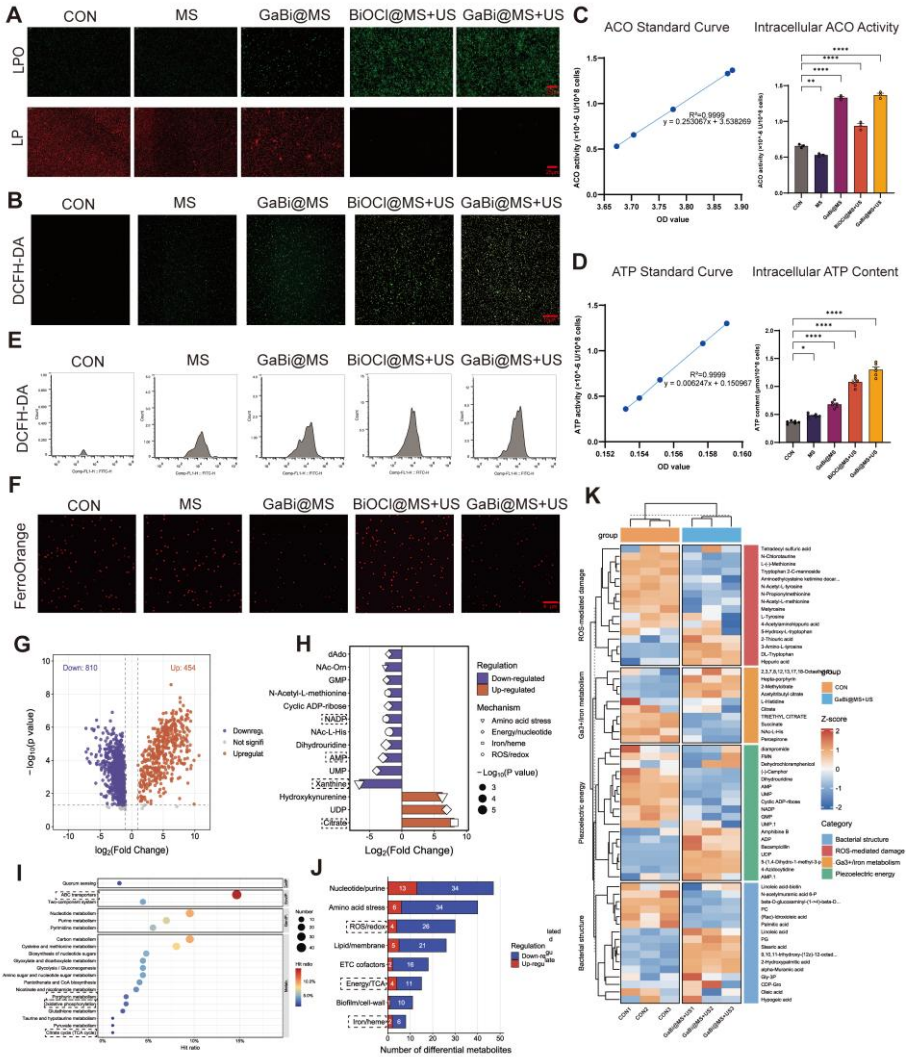


Fig. 3. Ultrasound-activated GaBi@MS couples oxidative injury with metabolic remodeling in MRSA. A Lipid-peroxidation-associated fluorescence after treatment. **B** Bacterial oxidant-associated fluorescence detected by DCFH-DA microscopy. **C** Aconitase assay calibration and quantified intracellular aconitase activity. **D** ATP assay calibration and intracellular ATP content. **E** Flow-cytometric DCF fluorescence distributions. **F** FerroOrange fluorescence as a readout of the bacterial labile Fe^{2+}-associated pool. **G** Volcano plot comparing CON with GaBi@MS+US, showing 1,264 differential metabolic features (454 increased and 810 decreased). **H** Representative annotated metabolites related to amino-acid, energy/nucleotide, iron/heme, membrane and redox processes. **I** Kyoto Encyclopedia of Genes and Genomes (KEGG) pathway-enrichment results. **J** Functional classification of differentially annotated metabolites. **K** Hierarchical clustering of representative metabolites. ATP, adenosine triphosphate; DCFH-DA, 2′,7′-dichlorodihydrofluorescein diacetate; DCF, 2′,7′-dichlorofluorescein. Quantitative bacterial assays were performed in at least three independent biological experiments; metabolomics comprised n = 3 independent biological samples per group. Quantitative data are shown as mean ± SD where error bars are displayed. Between-group statistical analyses for quantitative bacterial endpoints and metabolomic-feature identification are detailed separately in the Methods; metabolomic features were screened using VIP > 1 and $P < 0.05$.

GaBi@MS with ultrasound preserves osteoblast viability and osteogenic competence

We next assessed whether GaBi@MS+US preserves osteoblast viability and osteogenic competence. The concentration-response experiment showed that short-term MC3T3-E1 viability remained favorable from 25 to 250 μg/mL, with the highest relative viability observed around the 100 μg/mL working concentration. At 500 and 1000 μg/mL, viability was moderately reduced compared with the lower-dose conditions, defining a practical concentration window for subsequent experiments (Fig. 4C). In the time-course experiment performed at 100 μg/mL, all groups showed increasing metabolic activity from day 1 to day 7, and no sustained viability deficit was detected for GaBi@MS+US relative to the control condition at the measured time points (Fig. 4D). These data supported selection of 100 μg/mL for the mechanistic cell experiments.

Having established this favorable safety window, we then examined osteogenic function under bacteria-free conditions. ALP staining at day 7 and Alizarin Red S staining at day 14 remained readily detectable across all groups, without evidence of a gross loss of early osteogenic activity or mineralization-associated matrix deposition after GaBi@MS+US treatment (Fig. 4A). Western blotting likewise showed preservation of OPN and Runx2 expression across the material-treated groups (Fig. 4B), supporting maintenance of the osteogenic program at the protein level.

Cytoskeletal and transcription-factor imaging provided additional evidence that the treatment did not impair osteoblast phenotype. F-actin staining showed preserved cell spreading and filament organization after material exposure (Fig. 4F). Runx2 immunofluorescence remained evident in all groups and was highest in the GaBi@MS+US group in the corresponding quantitative analysis (Fig. 4G, I). These results were interpreted as preservation of osteogenic competence under the working treatment regimen rather than as proof of strong direct osteoinduction.

We finally tested osteoblast survival under direct infectious stress. MRSA challenge caused a pronounced loss of Calcein-AM-positive cells and a marked increase in PI-positive cells, reducing viability to a small fraction of the uninfected control. In contrast, cultures receiving GaBi@MS+US during MRSA challenge showed restoration of Calcein-AM-positive cell density and a marked reduction in PI positivity, with quantitative viability approaching the uninfected control level (Fig. 4E,

H). Thus, GaBi@MS+US combined bacteria-free cytocompatibility with preservation of osteoblast-lineage survival in an MRSA-rich environment, providing a repair-permissive cellular window for subsequent in vivo evaluation.

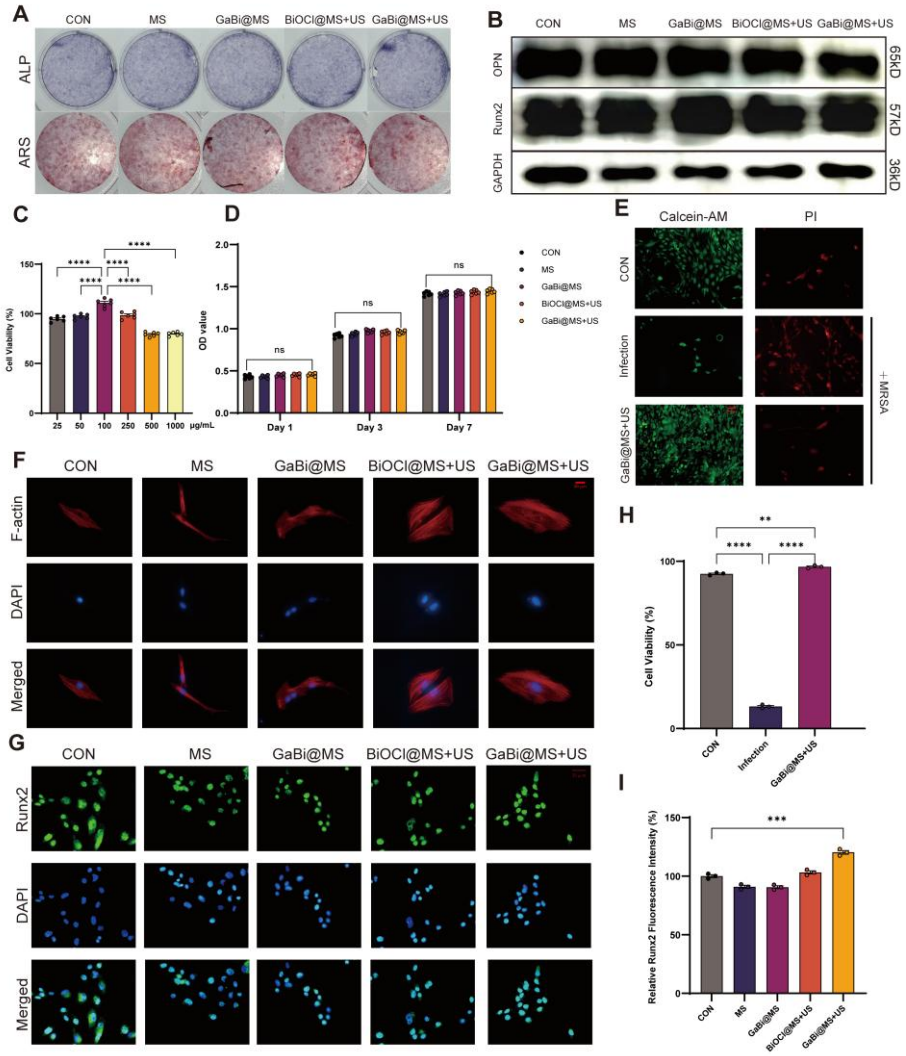


Fig. 4. GaBi@MS with ultrasound preserves osteoblast viability and osteogenic competence. A Alkaline phosphatase (ALP) staining at day 7 and Alizarin Red S (ARS) staining at day 14 under bacteria-free osteogenic conditions. **B** Immunoblot detection of osteopontin (OPN) and RUNX2, with GAPDH as loading control. **C** Cell viability following 24-h exposure to microspheres at the indicated concentrations (25–1,000 μg mL^{-1}). **D** Cell Counting Kit-8 (CCK-8) measurements on days 1, 3 and 7 at 100 μg mL^{-1}. **E** Calcein-AM/PI staining of uninfected, MRSA-infected and MRSA-infected plus GaBi@MS+US cultures. **F** F-actin and DAPI staining under bacteria-free conditions. **G** RUNX2 immunofluorescence. **H** Quantification of cell viability in the MRSA infection-challenge assay. **I** Quantification of RUNX2 fluorescence intensity. Images are representative of n = 3 independent cell experiments per condition; quantitative data are mean ± SD (n = 3 independent experiments). For single-endpoint group comparisons, one-way ANOVA with Tukey's multiple-comparisons test was used; time-dependent data were assessed by two-way ANOVA with multiple-comparison correction as described in the Methods. Brackets, where present, denote the groups compared. Significance: *P < 0.05, **P < 0.01, ***P < 0.001 and ****P < 0.0001; ns, not significant.

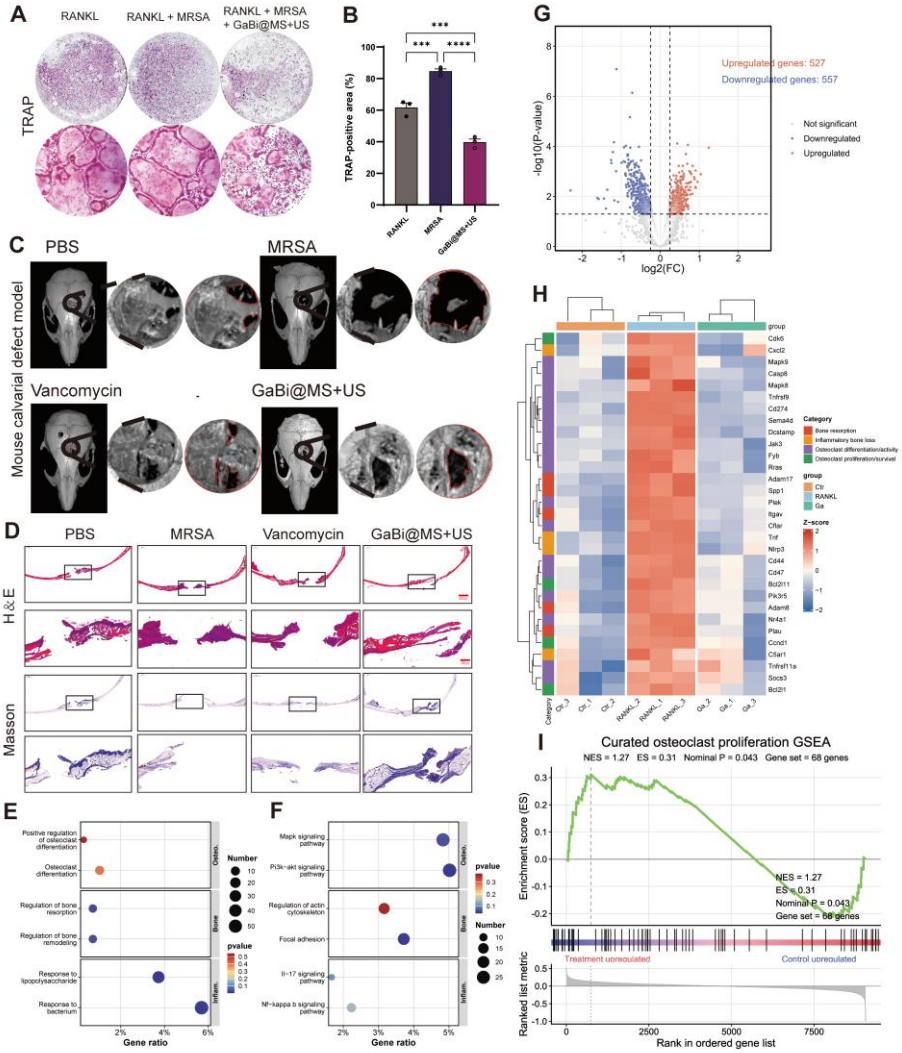
GaBi@MS with ultrasound attenuates infection-associated osteoclastogenesis and supports calvarial repair

We next examined whether the treatment could restrain infection-enhanced osteoclastogenesis. RANKL generated abundant TRAP-positive multinucleated osteoclast-like cells, and addition of MRSA further increased the TRAP-positive area. GaBi@MS+US markedly reversed this infection-associated increase, reducing both the density of TRAP staining and the proportion of the culture occupied by TRAP-positive cells (Fig. 5A, B). These findings indicate that the treatment acts not only on the bacterial compartment but also on the host resorptive response amplified by infection.

Figure 5 next evaluates the repair phenotype in the MRSA-inoculated calvarial-defect model. Micro-CT reconstruction showed a persistent, irregular residual defect in the untreated MRSA group, whereas the GaBi@MS+US group displayed greater continuity of the defect margin and more extensive mineralized bridging across the original defect region (Fig. 5C). Vancomycin produced an intermediate repair pattern. Histological evaluation was consistent with the imaging findings: H&E sections from the MRSA group showed poor tissue continuity within the defect, while GaBi@MS+US-treated defects contained more continuous repair tissue. Masson's trichrome staining further demonstrated more organized collagen deposition and matrix continuity after GaBi@MS+US treatment (Fig. 5D). These observations provide a complementary long-term repair readout in a cranial infected-defect setting.

To determine how GaBi@MS+US altered osteoclast-associated transcriptional programs, RNA sequencing was performed in the independent Ctrl-RANKL-Ga dataset, in which “Ga” denotes RANKL + GaBi@MS+US rather than free Ga or FAC treatment. GO enrichment highlighted processes related to osteoclast differentiation, regulation of bone resorption and remodeling, and inflammatory responses to bacterial or lipopolysaccharide-associated stimuli (Fig. 5E). KEGG analysis identified MAPK and PI3K-Akt signaling together with actin-cytoskeletal organization, focal adhesion, IL-17 signaling, and NF-κB signaling, linking the transcriptional response to both osteoclast differentiation and the cytoskeletal machinery required for mature resorptive function (Fig. 5F).

Differential-expression analysis of Ga versus RANKL identified 527 upregulated and 557 downregulated genes (Fig. 5G). The heatmap showed distinct clustering of Ctrl, RANKL, and Ga samples and broad reversal or attenuation of RANKL-associated expression patterns in genes related to bone resorption, inflammatory bone loss, osteoclast differentiation/activity, and osteoclast proliferation/survival (Fig. 5H). Consistent with these patterns, GSEA of the curated osteoclast-proliferation gene set showed enrichment in the treatment-associated direction (NES = 1.27, ES = 0.31, nominal P = 0.043; Fig. 5I). Taken together, Fig. 5 connects the reduction in MRSA-enhanced TRAP-positive osteoclast formation with broader remodeling of osteoclastogenic transcriptional programs and with improved structural repair in the infected calvarial-defect model.


A
RANKL
RANKL + MRSA
RANKL + MRSA + GaBi@MS+US
TRAP
B
TRAP-positive area (%)
RANKL
MRSA
GaBi@MS+US
C
PBS
MRSA
Vancomycin
GaBi@MS+US
Mouse calvarial defect model
D
PBS
MRSA
Vancomycin
GaBi@MS+US
H&E
Masson
E
Positive regulation of osteoclast differentiation
Osteoclast differentiation
Regulation of bone resorption
Regulation of bone remodeling
Response to lipopolysaccharide
Response to bacterium
Gene ratio
F
Mapk signaling pathway
Pi3k−akt signaling pathway
Regulation of actin cytoskeleton
Focal adhesion
Il−17 signaling pathway
Nf−kappa b signaling pathway
Gene ratio
G
Upregulated genes: 527
Downregulated genes: 557
Not significant
Downregulated
Upregulated
-log10(P-value)
log2(FC)
H
group
Category
Bone resorption
Inflammatory bone loss
Osteoclast differentiation/activity
Osteoclast proliferation/survival
Z-score
I
Curated osteoclast proliferation GSEA
NES = 1.27 ES = 0.31 Nominal P = 0.043 Gene set = 68 genes
Enrichment score (ES)
Treatment upregulated
Control upregulated
Ranked list metric
Rank in ordered gene list

535

Fig. 5. GaBi@MS with ultrasound attenuates infection-associated osteoclastogenesis and supports calvarial repair. A Tartrate-resistant acid phosphatase (TRAP) staining of RANKL, RANKL plus MRSA and RANKL plus MRSA plus GaBi@MS+US osteoclast cultures. **B** Quantified TRAP-positive area. **C** Micro-computed tomography (micro-CT) reconstructions of MRSA-inoculated calvarial defects in PBS, MRSA, vancomycin and GaBi@MS+US groups. **D** Hematoxylin–eosin (H&E) and Masson's trichrome staining of calvarial repair tissue. **E** Gene Ontology (GO) enrichment of the osteoclast RNA-sequencing (RNA-seq) dataset. **F** KEGG pathway enrichment in the same RNA-seq dataset. **G** Differential-expression volcano plot for Ga versus RANKL (527 upregulated and 557 downregulated genes). **H** Heatmap of selected osteoclast-associated genes in Ctrl, RANKL and Ga groups. **I** Gene set enrichment analysis (GSEA) for the curated osteoclast-proliferation gene set (nominal P = 0.043). RANKL, receptor activator of nuclear factor-κB ligand; in RNA-seq panels E–I, Ga indicates RANKL plus GaBi@MS+US, not free gallium or FAC treatment. Osteoclast cell assays comprised n = 3 independent experiments; RNA-seq comprised n = 3 independent biological samples per group. Representative calvarial images were obtained from n = 5 biologically independent mice per group. Data for the quantitative cell assay in B are mean ± SD and were compared by one-way ANOVA followed by Tukey's multiple-comparisons test. Significance symbols, when displayed, denote *P < 0.05, **P < 0.01, ***P < 0.001 and ****P < 0.0001.

GaBi@MS with ultrasound alters iron-associated signaling and mitochondrial potential in osteoclast cultures

To more directly interrogate the contribution of iron availability to osteoclast maturation, we established an FAC-conditioned iron-loading model (Fig. 6A). For clarity, "Ga" in this experiment denotes the complete GaBi@MS+US intervention; therefore, FAC + Ga indicates FAC-treated cells receiving GaBi@MS followed by US, and does not represent free Ga ions or a Ga-only treatment. DFO was included as an iron-chelation comparator.

FerroOrange imaging showed strong Fe^{2+}-associated fluorescence after FAC exposure. Addition of GaBi@MS+US markedly suppressed this signal, while DFO also reduced FerroOrange fluorescence but to a lesser extent than the Ga intervention (Fig. 6B). JC-1 flow cytometry showed that FAC shifted the mitochondrial membrane-potential profile toward a lower red/green state, whereas FAC + Ga produced a pronounced redistribution toward the high-potential population; DFO generated a partial recovery (Fig. 6C). Thus, reduction of the labile iron-associated signal after GaBi@MS+US was accompanied by recovery of mitochondrial membrane-potential status.

Western blotting then examined the canonical iron/osteoclast signaling axis. FAC increased TFR1, NFATC1, c-Fos, and TRAP expression relative to the baseline RANKL-induced condition, whereas FAC + Ga reduced all four proteins, with particularly marked suppression of TFR1, NFATC1, and TRAP. DFO produced a directionally similar but generally less pronounced response (Fig. 6D). Densitometric quantification confirmed these changes for each protein (Fig. 6E). TFR1 immunofluorescence independently reproduced the protein-level result: FAC increased TFR1-positive fluorescence, FAC + Ga strongly reduced it, and DFO partially lowered the signal (Fig. 6F).

Quantification of the JC-1 data showed a significant reduction in the red/green fluorescence ratio after FAC exposure and a marked increase after FAC + Ga, with DFO producing partial recovery (Fig. 6H). FerroOrange quantification showed the reciprocal pattern, with the highest relative fluorescence after FAC and the lowest value after FAC + Ga (Fig. 6G). Quantitative TFR1 fluorescence followed the same direction as the immunoblot, confirming suppression of iron-uptake-associated signaling by the GaBi@MS+US intervention (Fig. 6I).

Finally, intracellular Fe^{2+} content was quantified after normalization to total protein using the BCA standard curve (Fig. 6J). The colorimetric Fe^{2+} measurement did not show a significant difference between CON and FAC, whereas both FAC + Ga and FAC + DFO reduced intracellular Fe^{2+} relative to FAC; the reduction was greatest in FAC + Ga. The agreement between FerroOrange imaging, protein-normalized Fe^{2+} quantification, TFR1 measurements, mitochondrial potential, and osteoclastogenic proteins supports a model in which GaBi@MS+US constrains iron-supported osteoclast maturation while restoring mitochondrial functional status.

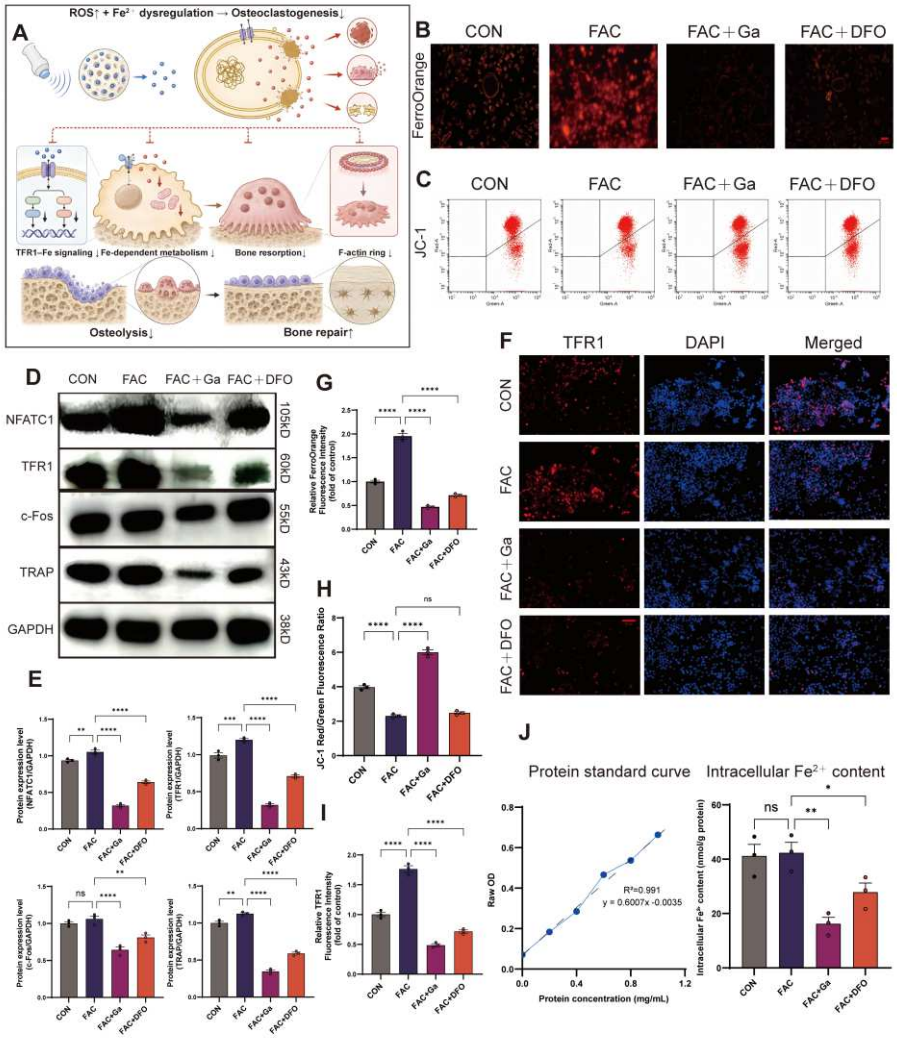


Fig. 6. GaBi@MS with ultrasound alters iron-associated signaling and mitochondrial potential in osteoclast cultures. A Schematic representation of ferric ammonium citrate (FAC)-conditioned iron loading and treatment. **B** FerroOrange images reporting labile Fe^{2+}-associated fluorescence in CON, FAC, FAC + Ga and FAC + DFO groups. **C** JC-1 flow-cytometry profiles of mitochondrial membrane potential. **D** Immunoblots for NFATC1, TFR1, c-Fos and TRAP, with GAPDH as the loading control. **E** Corresponding immunoblot densitometry normalized to GAPDH. **F** TFR1 immunofluorescence with DAPI nuclear counterstaining. **G** Quantification of FerroOrange fluorescence. **H** Quantification of the JC-1 aggregate/monomer fluorescence ratio. **I** Quantification of TFR1 immunofluorescence. **J** Bicinchoninic acid (BCA) assay standard curve and protein-normalized intracellular Fe^{2+} content. DFO, deferoxamine; TFR1, transferrin receptor 1; NFATC1, nuclear factor of activated T cells 1; TRAP, tartrate-resistant acid phosphatase. Ga denotes GaBi@MS+US, not free Ga ions; FAC + Ga denotes FAC-treated cells receiving GaBi@MS+US. Representative images and immunoblots derive from n = 3 independent cell experiments. Quantitative cell data in E and G–J (excluding the calibration series in J) are mean ± SD (n = 3 independent experiments). Group comparisons were analyzed by one-way ANOVA followed by Tukey's multiple-comparisons test as described in the Methods. Brackets show the groups compared; *P < 0.05, **P < 0.01, ***P < 0.001 and ****P < 0.0001; ns, not significant.

GaBi@MS with ultrasound suppresses osteoclast maturation and shifts iron-associated transcriptional programs

We next assessed the mature osteoclast phenotype under the same iron-loading conditions. Whole-well TRAP staining showed extensive osteoclast formation in CON and FAC cultures, whereas FAC + Ga markedly reduced the TRAP-positive area. DFO also suppressed TRAP staining, producing a directionally convergent phenotype (Fig. 7A). F-actin staining provided a complementary maturation readout: large peripheral actin rings were readily observed in the iron-loaded cultures, while GaBi@MS+US markedly reduced the number and integrity of these ring structures; DFO again produced a partial suppressive effect (Fig. 7B). Because formation of the peripheral actin ring is a defining cytoskeletal feature of mature resorptive osteoclasts, these findings indicate that the intervention limits both differentiation-associated TRAP activity and acquisition of the mature resorptive cytoskeleton.

The independent Ctrl-RANKL-Ga transcriptomic dataset was then examined for iron- and osteoclast-related programs. The heatmap showed a broad RANKL-associated shift in genes involved in iron uptake/transport, iron storage/regulation, iron-related stress, heme metabolism, and mitochondrial iron handling, with the Ga group displaying partial reversal or reorganization of many of these changes (Fig. 7C). Functional enrichment identified phagocytosis, lysosome biogenesis, autophagy, ferroptosis-related pathways, HIF-1 signaling, mineral absorption, and other iron/osteoclast-associated processes (Fig. 7D). These enrichments were used as pathway-level context rather than as independent proof of a specific iron target because several signals were exploratory and FAC-treated cells were not sequenced.

Selected-gene analysis further illustrated coordinated changes in iron-handling and redox-related genes, including Slc40a1, Hif1a, Slc25a37, Slc11a2, Fth1, Gpx4, Acsl4, Tfrc, Ncoa4, Hmox2, Ireb2, and Cp (Fig. 7E). The curated osteoclast iron-metabolism GSEA showed only a directional, non-significant shift (NES = -1.05, ES = -0.27, nominal P = 0.201; Fig. 7F). Accordingly, the transcriptomic findings were interpreted as supportive, hypothesis-generating context for the biochemical and phenotypic data rather than direct transcriptional validation of the FAC intervention.

627 Across Figs. 6 and 7, the strongest mechanistic evidence therefore comes from the convergence of
628 labile-iron-associated fluorescence, protein-normalized Fe^{2+} content, TFR1 signaling, mitochondrial
629 membrane potential, osteoclastogenic protein expression, TRAP staining, and F-actin-ring formation.

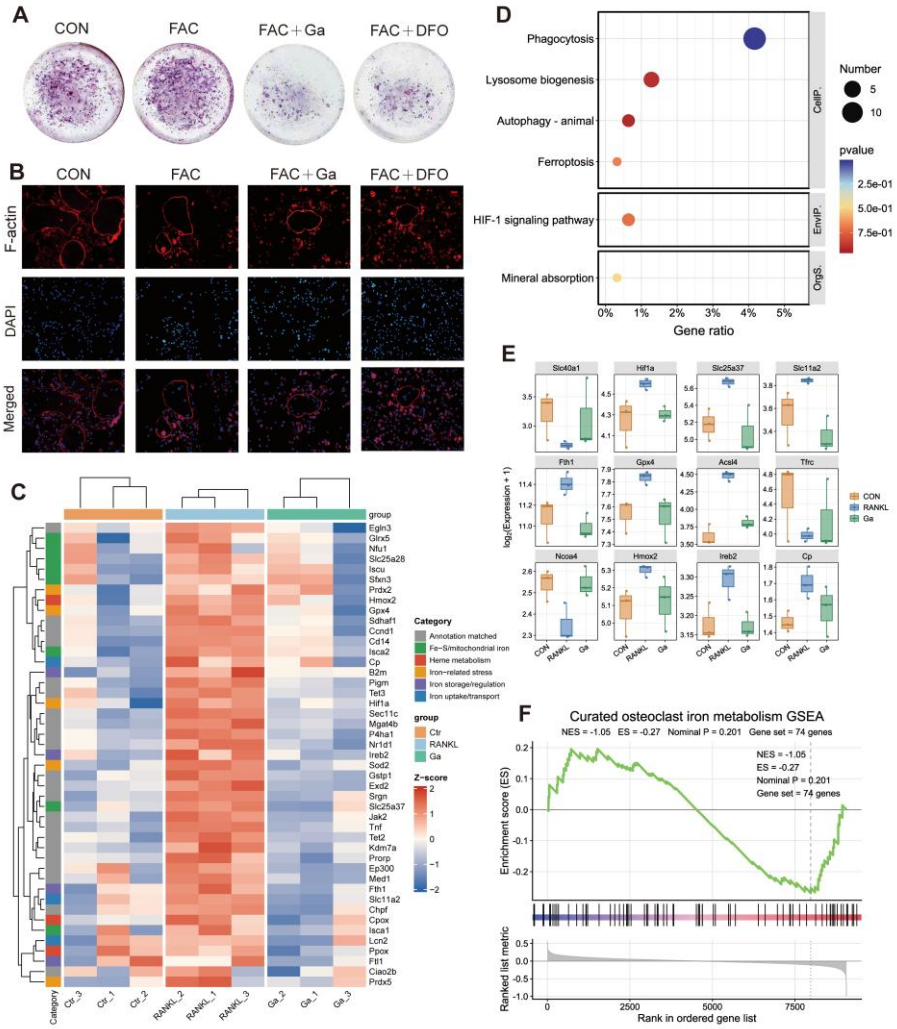


Fig. 7. GaBi@MS with ultrasound suppresses osteoclast maturation and shifts iron-associated transcriptional programs. A Whole-well TRAP staining of RANKL-induced CON, FAC, FAC + Ga and FAC + DFO cultures. **B** F-actin/DAPI images of peripheral actin-ring organization. **C** Heatmap of osteoclast- and iron-metabolism-associated transcripts in the independent Ctrl–RANKL–Ga RNA-seq dataset. **D** Pathway-enrichment analysis of iron-handling, phagolysosomal, autophagic, ferroptosis-associated and osteoclastogenic processes. **E** Selected genes grouped by iron-metabolic or osteoclast-related function. **F** GSEA for the curated osteoclast iron-metabolism set (nominal P = 0.201; not statistically significant). TRAP, tartrate-resistant acid phosphatase; DAPI, 4′,6-diamidino-2-phenylindole. In A and B, Ga denotes GaBi@MS+US in FAC-conditioned cultures. Panels C–F derive from the independent Ctrl, RANKL and Ga RNA-seq experiment, in which Ga denotes RANKL plus GaBi@MS+US; FAC-treated cells were not sequenced. Images in A and B are representative of n = 3 independent cell experiments; RNA-seq included n = 3 independent biological samples per group. Differential-expression and pathway-enrichment analyses followed the procedures described in the Methods.

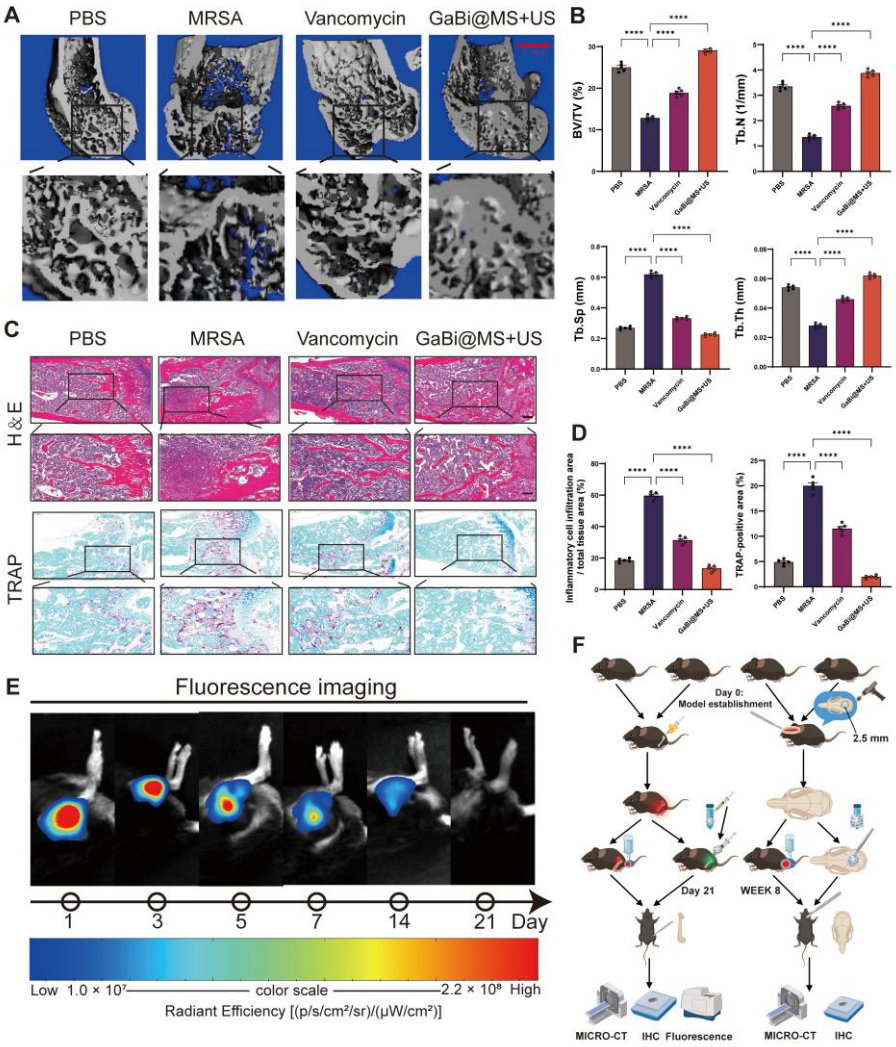
GaBi@MS with ultrasound limits inflammatory osteolysis in murine femoral osteomyelitis

The therapeutic performance of the platform was next evaluated in the 21-day femoral osteomyelitis model (Fig. 8). Three-dimensional micro-CT reconstruction showed preserved trabecular structure in the PBS group, extensive local bone destruction in the MRSA group, partial preservation after vancomycin, and substantially improved trabecular continuity after GaBi@MS+US treatment (Fig. 8A). Quantitative microarchitectural analysis confirmed this pattern: relative to untreated MRSA infection, GaBi@MS+US increased BV/TV, trabecular number, and trabecular thickness while reducing trabecular separation (Fig. 8B). The direction of change across all four parameters was consistent with preservation of local bone architecture rather than improvement in a single isolated metric.

Histological analysis further demonstrated attenuation of infection-associated tissue injury. H&E sections from MRSA-infected femora contained dense inflammatory-cell infiltration and marked disruption of normal marrow and trabecular architecture. These changes were reduced in the vancomycin group and were further attenuated after GaBi@MS+US, with better preservation of bone and marrow organization (Fig. 8C). TRAP staining showed extensive osteoclast-associated signal in the MRSA group, whereas the GaBi@MS+US group displayed markedly less TRAP-positive tissue. Quantitative analysis confirmed significant reductions in both inflammatory-cell infiltration and TRAP-positive area after GaBi@MS+US relative to untreated infection (Fig. 8D).

Longitudinal fluorescence imaging of Cy5-labeled PLGA microspheres was performed to assess local carrier retention and the temporal decline of material-associated signal at the femoral site. Representative images showed a progressive decrease in Cy5-associated fluorescence from day 1 to day 21 after local administration, consistent with reduced local persistence of the labeled PLGA carrier and providing an indirect indication of material degradation and/or clearance rather than bacterial burden (Fig. 8E; Figure S13). The fluorescence color scale represents radiant efficiency. The femoral osteomyelitis and calvarial-defect models and their respective collection endpoints on day 21 and at week 8 are summarized in Fig. 8F; the administration and US schedules are detailed in the Methods.

669 Together, the micro-CT, H&E, and TRAP data demonstrate that local GaBi@MS+US simultaneously
670 reduces the infection-associated inflammatory phenotype and restrains osteolytic bone loss in vivo.


A
PBS
MRSA
Vancomycin
GaBi@MS+US
B
BV/TV (%)
Tb.N (1/mm)
Tb.Sp (mm)
Tb.Th (mm)
C
H&E
TRAP
D
Inflammatory cell infiltration area / total tissue area (%)
TRAP-positive area (%)
E
Fluorescence imaging
1
3
5
7
14
21
Day
Low 1.0 × 10⁷
color scale
2.2 × 10⁸ High
Radiant Efficiency [(p/s/cm²/sr)/(μW/cm²)]
F
Day 0:
Model establishment
2.5 mm
Day 21
WEEK 8
MICRO-CT
IHC
Fluorescence
MICRO-CT
IHC

671

Fig. 8. GaBi@MS with ultrasound limits inflammatory osteolysis in murine femoral osteomyelitis. A Micro-CT reconstruction of femora harvested on day 21, with representative regions of interest. **B** Bone volume fraction (BV/TV), trabecular number (Tb.N), trabecular separation (Tb.Sp) and trabecular thickness (Tb.Th). **C** H&E and TRAP-stained femoral sections. **D** Quantified inflammatory-cell infiltration and TRAP-positive area. **E** Longitudinal fluorescence images of Cy5-labeled PLGA microspheres at the femoral site on days 1, 3, 5, 7, 14 and 21, used to follow local carrier persistence and the degradation/clearance trend rather than bacterial burden; the pseudocolor scale indicates radiant efficiency, from 1.0×10^7 to 2.2×10^8 [(photons s^{-1} cm^{-2} sr^{-1})/(μW cm^{-2})]. **F** Schematic of femoral osteomyelitis and MRSA-inoculated calvarial-defect models, with collection at day 21 and week 8, respectively. PBS, phosphate-buffered saline; H&E, hematoxylin–eosin; TRAP, tartrate-resistant acid phosphatase. Experimental groups were PBS, MRSA, vancomycin and GaBi@MS+US. Representative images correspond to n = 5 biologically independent mice per group. Endpoint measurements in B and D are shown as mean ± SD (n = 5 independent mice per group) and analyzed using one-way ANOVA followed by Tukey's multiple-comparisons test. Longitudinal carrier tracking in E includes repeated observations of the same five mice (n = 5); the longitudinal statistical analysis is described in the Methods. Brackets, where shown, denote comparisons; *P < 0.05, **P < 0.01, ***P < 0.001 and ****P < 0.0001.

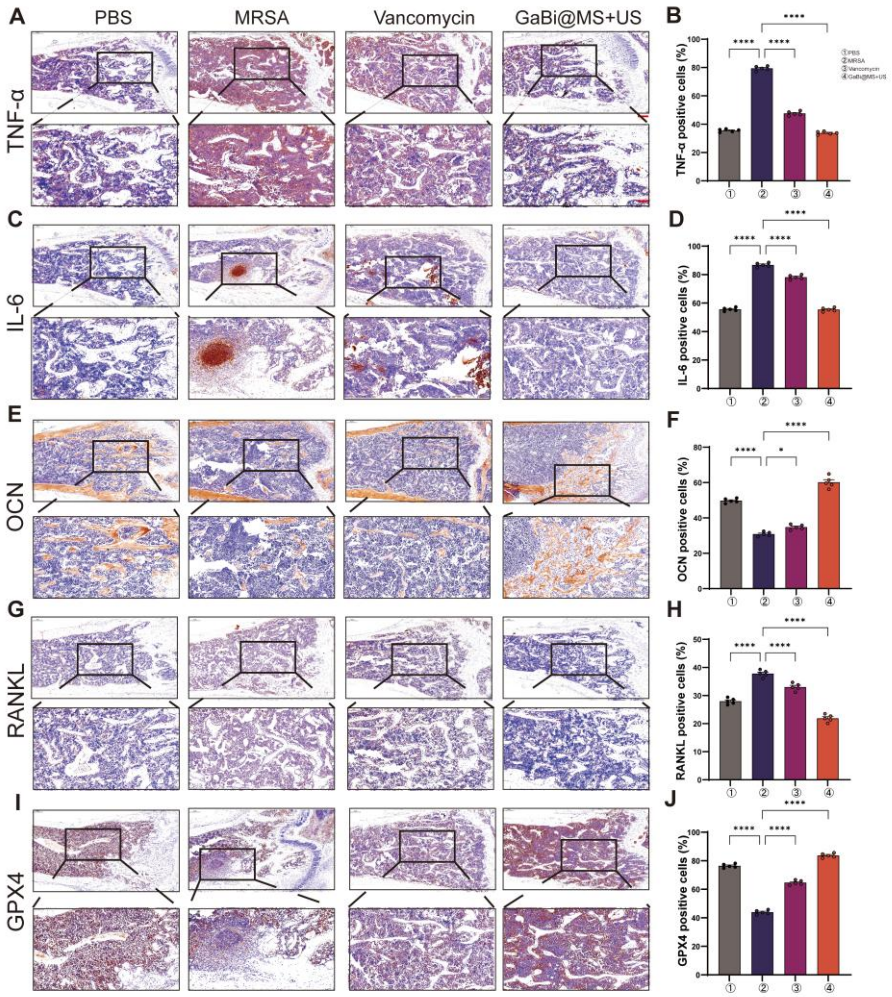
GaBi@MS with ultrasound changes inflammatory, osteogenic, osteoclastogenic and redox-associated markers in infected bone

To characterize the tissue microenvironment accompanying the structural protection observed in Fig. 8, femoral sections collected on day 21 were examined for TNF-α, IL-6, OCN, RANKL, and GPX4. Representative immunohistochemical images and corresponding enlarged regions are shown for each marker, together with quantification of the percentages of immunopositive cells. MRSA infection increased the percentages of TNF-α- and IL-6-positive cells relative to the uninfected PBS group (Fig. 9A–D). Vancomycin reduced both inflammatory readouts, whereas GaBi@MS+US produced a greater reduction, with positive-cell percentages approaching those in the PBS group. These changes were consistent with the lower inflammatory-cell infiltration observed by H&E staining.

The osteogenic and osteoclastogenic markers displayed reciprocal treatment-associated changes. The percentage of OCN-positive cells was lower in the MRSA group than in PBS, whereas GaBi@MS+US increased OCN positivity relative to untreated infection and vancomycin (Fig. 9E, F). Conversely, MRSA increased the percentage of RANKL-positive cells, and GaBi@MS+US reduced this

osteoclast-supportive signal relative to both infected comparator groups (Fig. 9G, H). Together with the micro-CT and TRAP findings, the higher OCN and lower RANKL readouts were consistent with preservation of the bone-forming compartment and attenuation of infection-associated osteoclastogenic signaling. The tissue-level OCN response does not by itself establish a direct osteoinductive action of the material.

MRSA infection also reduced the percentage of GPX4-positive cells, whereas vancomycin partially restored this readout and GaBi@MS+US showed the greatest preservation among the infected groups (Fig. 9I, J). GPX4 was interpreted as a tissue redox-protective marker rather than as stand-alone evidence of ferroptosis regulation. Considered alongside the lower TNF-α, IL-6, and RANKL positivity, higher OCN positivity, reduced TRAP-positive area, and improved bone microarchitecture, these findings support a less inflammatory and less osteolytic tissue environment after GaBi@MS+US treatment. The immunohistochemical measurements describe tissue-level marker changes and do not identify the specific cell types responsible for the GPX4 response.



714
715 **Fig. 9. GaBi@MS with ultrasound changes inflammatory, osteogenic, osteoclastogenic and redox-associated**
716 **markers in infected bone. A** Representative TNF-α immunohistochemistry of femoral sections at day 21. **B**
717 Quantification of TNF-α-positive cells. **C** Representative IL-6 immunohistochemistry. **D** Quantification of IL-6-
718 positive cells. **E** Representative osteocalcin (OCN) immunohistochemistry. **F** Quantification of OCN-positive cells. **G**
719 Representative RANKL immunohistochemistry. **H** Quantification of RANKL-positive cells. **I** Representative
720 glutathione peroxidase 4 (GPX4) immunohistochemistry. **J** Quantification of GPX4-positive cells. Quantitative values
721 are percentages of positive cells within the analyzed sections. Numbered labels 1–4, where displayed, indicate PBS,
722 MRSA, vancomycin and GaBi@MS+US, respectively. Enlarged regions correspond to the boxed areas of the
723 representative images. GPX4 is a tissue redox-associated marker and is not presented as a stand-alone readout of
724 ferroptosis. Images represent n = 5 biologically independent mice per group; quantitative data are mean ± SD (n = 5
725 independent mice per group). Groupwise comparisons used one-way ANOVA followed by Tukey's multiple-
726 comparisons test; brackets identify comparisons where present. *P < 0.05, **P < 0.01, ***P < 0.001 and ****P <
727 0.0001.

Discussion

MRSA-associated osteomyelitis is difficult to resolve because persistent infection and host bone destruction are mechanistically coupled. Biofilm-protected bacteria sustain inflammatory signaling, while the resulting microenvironment promotes RANKL-dependent osteoclastogenesis and compromises skeletal repair [1, 2, 3, 4, 5, 20]. The central objective of this study was therefore not simply to develop another local antibacterial material, but to interrupt this pathogen–host feedback loop. The data support a unified sequence in which porous PLGA microspheres localize an US-responsive BiOCl-Ga phase; non-invasive US triggers piezocatalytic oxidative injury; Ga-associated iron interference broadens the stress imposed on MRSA and constrains iron-supported osteoclast maturation; and preservation of the osteoblast compartment allows the lesion to transition toward a repair-permissive state.

The material architecture is integral to the therapeutic mechanism. Ga incorporation preserved the principal BiOCl crystalline framework, indicating that Ga was accommodated within the host lattice rather than forming a separate phase. This structural retention is essential, because it allows the electronic benefit of doping, a narrowed band gap, to be realized without sacrificing the crystalline integrity on which piezoelectric charge separation depends. The narrowed band gap implies more efficient charge generation under US, which is consistent with the enhanced piezoelectric current and potential responses observed for GaBi@MS relative to BiOCl@MS. The reduced interfacial charge transfer resistance after US irradiation further suggests that Ga doping facilitates charge separation and migration rather than merely increasing charge generation, which is a prerequisite for converting mechanical stimuli into usable redox chemistry.

Critically, this piezocatalytic activity persisted after encapsulation. The ability of GaBi@MS to drive DPBF consumption and TMB oxidation under US indicates that the porous PLGA matrix does not block access of the reactive species to the surrounding medium, but instead serves as a structurally permissive carrier that preserves the catalytic interface of the two-dimensional nanosheets. In this configuration, the nanosheet phase defines the catalytic function, whereas the microsphere format defines the delivery function. This division of roles is the basis of the spatiotemporal control exploited

here: the microsphere confines the active phase to the lesion site, while US determines when catalysis is switched on.[25–27] Such control is particularly relevant to deep musculoskeletal infection, where repeated surgical access is impractical and passive local depots cannot be externally regulated after implantation [6–11, 23, 24, 28–31].

The antibacterial phenotype is best explained by convergence of piezocatalytic oxidative injury and Ga-associated iron/metabolic stress. BiOCl@MS+US alone produced substantial membrane damage, supporting US-triggered piezocatalysis as a major effector. In the Ga-containing treatment, increased DCFH-DA and lipid-peroxidation-associated signals coincided with membrane and ultrastructural injury, reduced biofilm biomass, and persistent suppression of colony recovery. Because *S. aureus* depends on iron and heme for respiration, central metabolism, redox homeostasis, and virulence [12, 13, 14, 15, 16], Ga-mediated interference provides a complementary constraint [12, 13, 16, 21, 22]. The reduced FerroOrange-associated labile-iron signal and changes in porphyrin/heme, TCA-cycle, glutathione, nucleotide, membrane-lipid, and transport pathways are consistent with network-level iron/metabolic disturbance. The increases in aconitase activity and ATP, when considered together with impaired colony recovery and structural injury, are more consistent with a compensatory or dysregulated metabolic state than improved bacterial fitness [14, 32, 33]. Because intracellular Ga, Ga–protein binding, and formal combination indices were not measured, the data support mechanistic convergence rather than a specific molecular target or formally quantified pharmacological synergy.

Iron dependence also links the pathogen to the host osteoclast compartment. MRSA enhanced RANKL-induced TRAP positivity, whereas GaBi@MS+US attenuated this phenotype. In FAC-conditioned cultures, GaBi@MS+US reduced labile Fe^{2+}, FerroOrange and TFR1 signals, c-Fos/NFATC1/TRAP expression, and mature F-actin-ring formation; DFO produced a broadly convergent response. These findings are consistent with evidence that TFR1-mediated iron uptake supports osteoclast mitochondrial and cytoskeletal programs [18] and that iron chelation suppresses osteoclast differentiation and electron-transport-chain activity [19]. The independent Ctrl-RANKL-Ga RNA-seq dataset provided pathway-level context, but FAC-treated cells were not sequenced and the curated iron-metabolism GSEA was not statistically significant (nominal P = 0.201); these

transcriptomic results should therefore be regarded as supportive and exploratory rather than direct validation of the FAC intervention.

At 100 μg/mL, GaBi@MS+US did not cause a sustained reduction in MC3T3-E1 viability and preserved F-actin organization, OPN/Runx2 expression, ALP staining, and mineralization-associated staining. Under MRSA challenge, treatment also preserved osteoblast-lineage cell viability. In vivo, Cy5-labeled PLGA fluorescence declined over time, while GaBi@MS+US reduced inflammatory infiltration, TRAP activity, and TNF-α, IL-6, and RANKL staining and preserved trabecular architecture; the infected calvarial-defect model further showed improved tissue bridging and collagen organization. These findings support a repair-permissive effect arising from infection control, restraint of pathological osteoclastogenesis, and preservation of the osteoblast compartment rather than a claim of strong direct osteoinduction. The vancomycin group served as a clinically relevant benchmark [34], but the study was not designed to establish superiority over standard antibiotic therapy and did not include quantitative viable bacterial recovery from bone.

Several limitations remain. Ga-release kinetics, local Ga exposure, pharmacokinetics, biodistribution, PLGA degradation, long-term systemic safety, and quantitative acoustic dosimetry were not determined. Direct Ga-uptake and target-engagement studies, respiratory-flux assays, osteoclast resorption-pit analysis, validation in primary osteoclast precursors, quantitative bacterial recovery from bone, larger cohorts, and longer follow-up would strengthen the mechanistic and translational framework. Within these limits, the present data support a locally delivered, externally activated platform that couples piezocatalytic antibacterial activity with iron-sensitive regulation of the pathogen–osteoclast axis while preserving osteoblast competence.

Conclusions

In summary, we developed Ga-doped BiOCl piezocatalytic microspheres (GaBi@MS) that integrate ultrasound-triggered piezocatalysis with Ga-mediated iron metabolism interference for the treatment of MRSA bone infections. Ga doping narrowed the band gap and enhanced piezocatalytic ROS generation, while gallium-associated changes were consistent with interference in bacterial iron handling. Under US stimulation, GaBi@MS effectively killed MRSA, disrupted biofilms, and

alleviated infection-associated inflammation and osteolysis. Notably, GaBi@MS suppressed MRSA-enhanced osteoclastogenesis by reducing labile iron and TFR1/c-Fos/NFATC1/TRAP signaling, while preserving osteoblast function. In murine osteomyelitis and infected calvarial-defect models, GaBi@MS+US reduced infection-associated signals, attenuated osteoclast activity, and preserved bone architecture, supporting bone repair. This work establishes a dual-mechanism piezocatalytic platform that couples oxidative antibacterial action with iron-sensitive regulation of the pathogen-osteoclast axis, offering a promising strategy for recalcitrant MRSA bone infections.

Supporting Information

Additional X-ray photoelectron spectroscopy, X-ray diffraction, zeta-potential, thermogravimetric, and electrochemical characterization; quantitative antibacterial and antibiofilm assays; bacterial oxidative, lipid-peroxidation, and iron-associated measurements; osteoblast and osteoclast analyses; and longitudinal in vivo fluorescence measurements (Figures S1–S14).

Declarations

Ethics approval and consent to participate

All animal procedures were reviewed and approved by the Institutional Animal Care and Use Committee of Shandong First Medical University (Approval No. 2025-073) and were conducted in accordance with approved institutional guidelines for the care and use of laboratory animals. Animals were housed under specific-pathogen-free conditions. Anesthesia, postoperative monitoring, humane endpoints, and euthanasia followed the approved protocol, and all efforts were made to minimize animal suffering and the number of animals used.

Consent for publication

Not applicable.

Availability of data and materials

The data supporting the findings of this study, including numerical source data underlying the figures, uncropped western blot images, image-quantification files, and micro-CT source data, are available

from the corresponding authors upon reasonable request. The RNA-sequencing and untargeted metabolomics datasets will be deposited in appropriate public repositories; accession numbers and reviewer-access information will be provided during peer review and included in the published article once available.

COMPETING INTERESTS

The authors declare no competing interests.

Funding

This work was supported by the National Natural Science Foundation of China (grant no. 82002325), the Natural Science Foundation of Shandong Province (ZR2025LSW042 and 2025KJHZ018), and the Shandong Provincial Medical Association (YXH2025YS068 and YXH2024YS019).

Authors' contributions

Z. Xie curated and validated the data and wrote the original draft.

T. Li contributed to conceptualization and methodology.

C. Sun contributed to methodology.

C. Zeng investigated, curated and validated the data.

X. Jing contributed to investigation.

C. Liu curated the data.

J. Ma curated the data and contributed to investigation and methodology.

T. Ning curated the data.

Z. Xu curated the data.

J. Dong contributed to conceptualization, funding acquisition and supervision.

Z. Dong contributed to conceptualization, methodology, supervision and manuscript review and editing.

X. Xu contributed to conceptualization, supervision and manuscript review and editing.

Acknowledgements

Not applicable.

References

1. Urish KL, Cassat JE. *Staphylococcus aureus* Osteomyelitis: Bone, Bugs, and Surgery. Infect Immun. 2020;88:e00932-19.

2. Song M, Sun J, Lv K, Li J, Shi J, Xu Y. A comprehensive review of pathology and treatment of *Staphylococcus aureus* osteomyelitis. Clin Exp Med. 2025;25:131.

3. Wu H, Jia C, Wang X, Shen J, Tan J, Wei Z, Wang S, Sun D, Xie Z, Luo F. The impact of methicillin resistance on clinical outcome among patients with *Staphylococcus aureus* osteomyelitis: a retrospective cohort study of 482 cases. Sci Rep. 2023;13:7990.

4. Nishizawa M, Djurasovic M, Glassman SD, Crawford CH III, Dimar JR II, Owens RK II, Mathew J, Kostic B, Carreon LY. Clinical characteristics and surgical outcomes of spinal infection caused by methicillin-resistant *Staphylococcus aureus*. Spine J. 2026;26:272–279.

5. Wang X, Wang S, Fu J, Sun D, Shen J, Xie Z. Risk factors associated with recurrence of extremity osteomyelitis treated with the induced membrane technique. Injury. 2020;51:307–311.

6. Cheng S, Meng XH, Li Z, Han HH, Zhang YF. Nanomaterial-mediated antibiotic delivery: a novel strategy for osteomyelitis therapy. Front Bioeng Biotechnol. 2025;13:1671151.

7. Wassif RK, Elkayal M, Shamma RN, Elkheshen SA. Recent advances in the local antibiotics delivery systems for management of osteomyelitis. Drug Delivery. 2021;28:2392–2414.

8. Cahill SV, Kwon H-K, Back J, Lee I, Lee S, Alder KD, Hao Z, Yu KE, Dussik CM, Kyriakides TR, Lee FY. Locally delivered adjuvant biofilm-penetrating antibiotics rescue impaired endochondral fracture healing caused by MRSA infection. J Orthop Res. 2021;39:402–414.

9. Tao J, Zhang Y, Shen A, Yang Y, Diao L, Wang L, Cai D, Hu Y. Injectable Chitosan-Based Thermosensitive Hydrogel/Nanoparticle-Loaded System for Local Delivery of Vancomycin in the Treatment of Osteomyelitis. Int J Nanomed. 2020;15:5855–5871.

10. Posadowska U, Brzychczy-Włoch M, Drożdż A, Krok-Borkowicz M, Włodarczyk-Biegun M, Dobrzyński P, Chrzanowski W, Pamuła E. Injectable hybrid delivery system composed of gellan gum,

885 nanoparticles and gentamicin for the localized treatment of bone infections. Expert Opin Drug Deliv.
886 2016;13:613–620.
887 11. Bezstarosti H, Metsemakers WJ, van Lieshout EMM, Voskamp LW, Kortram K, McNally MA, Marais
888 LC, Verhofstad MHJ. Management of critical-sized bone defects in the treatment of fracture-related
889 infection: a systematic review and pooled analysis. Arch Orthop Trauma Surg. 2021;141:1215–1230.
890 12. Goss CH, Kaneko Y, Khuu L, Anderson GD, Ravishankar S, Aitken ML, Lechtzin N, Zhou G, Czyz
891 DM, McLean K, Olakanmi O, Shuman HA, Teresi M, Wilhelm E, Caldwell E, Salipante SJ, Hornick
892 DB, Siehnel RJ, Becker L, Britigan BE, et al. Gallium disrupts bacterial iron metabolism and has
893 therapeutic effects in mice and humans with lung infections. Sci Transl Med. 2018;10:eaat7520.
894 13. Choi SR, Hassan MA, Britigan BE, Narayanasamy P. Antimicrobial activity of gallium(III)
895 compounds: pathogen-dependent targeting of multiple iron/heme-dependent biological processes. Curr
896 Issues Mol Biol. 2024;46:9149–9161.
897 14. Friedman DB, Stauff DL, Pishchany G, Whitwell CW, Torres VJ, Skaar EP. *Staphylococcus aureus*
898 redirects central metabolism to increase iron availability. PLoS Pathog. 2006;2:e87.
899 15. Dale SE, Doherty-Kirby A, Lajoie G, Heinrichs DE. Role of siderophore biosynthesis in virulence of
900 *Staphylococcus aureus*: identification and characterization of genes involved in production of a
901 siderophore. Infect Immun. 2004;72:29–37.
902 16. Bernstein LR. Mechanisms of therapeutic activity for gallium. Pharmacol Rev. 1998;50:665–682.
903 17. Wang X, Chen B, Sun J, Jiang Y, Zhang H, Zhang P, Fei B, Xu Y. Iron-induced oxidative stress
904 stimulates osteoclast differentiation via NF-κB signaling pathway in mouse model. Metabolism.
905 2018;83:167–176.
906 18. Das BK, Wang L, Fujiwara T, Zhou J, Aykin-Burns N, Krager KJ, Lan R, Mackintosh SG, Edmondson
907 R, Jennings ML, Wang X, Feng JQ, Barrientos T, Gogoi J, Kannan A, Gao L, Xing W, Mohan S, Zhao
908 H. Transferrin receptor 1-mediated iron uptake regulates bone mass in mice via osteoclast
909 mitochondria and cytoskeleton. eLife. 2022;11:e73539.
910 19. Zhang J, Hu W, Ding C, Yao G, Zhao H, Wu S. Deferoxamine inhibits iron-uptake-stimulated
911 osteoclast differentiation by suppressing electron transport chain and MAPK signaling. Toxicol Lett.
912 2019;313:50–59.

913 20. Ren L-R, Wang Z-H, Wang H, He X-Q, Song M-G, Xu Y-Q. *Staphylococcus aureus* induces
914 osteoclastogenesis via the NF-κB signaling pathway. Med Sci Monit. 2017;23:4579–4590.
915 21. Bonchi C, Imperi F, Minandri F, Visca P, Frangipani E. Repurposing of gallium-based drugs for
916 antibacterial therapy. BioFactors. 2014;40:303–312.
917 22. Mohammad Hanifeh N, Keyvani-Ghamsari S, Khorsandi K, Mahmoodi Khaledi E. Effect of gallium
918 nitrate on the antibacterial activity of vancomycin in methicillin-sensitive and resistant *Staphylococcus*
919 *aureus*. Arch Microbiol. 2024;206:304.
920 23. He J, Lin X, Zhang D, Hu H, Chen X, Xu F, Zhou M. Wake biofilm up to enhance suicidal uptake of
921 gallium for chronic lung infection treatment. Biomaterials. 2024;310:122619.
922 24. Gu C, Zhang X, Hu Y, Li Z, Li J, Zhou Y. Ga-doped polydopamine coating on Ti implants for
923 enhanced antibacterial and osteogenic activity. Mater Lett. 2026;407:140020.
924 25. Vinikoor T, Dzidotor GK, Le TT, Liu Y, Kan H-M, Barui S, Chorsi MT, Curry EJ, Reinhardt E, Wang
925 H, Singh P, Merriman MA, D'Orio E, Park J, Xiao S, Chapman JH, Lin F, Truong C-S, Prasadh S,
926 Chuba L, et al. Injectable and biodegradable piezoelectric hydrogel for osteoarthritis treatment. Nat
927 Commun. 2023;14:6257.
928 26. Zhao Y, Liu Y, Liao R, Ran P, Liu Y, Li Z, Shao J, Zhao L. Biofilm Microenvironment-Sensitive
929 Piezoelectric Nanomotors for Enhanced Penetration and ROS/NO Synergistic Bacterial Elimination.
930 ACS Appl Mater Interfaces. 2024;16:3147–3161.
931 27. Sengupta D, Naskar S, Mandal D. Reactive oxygen species for therapeutic application: Role of
932 piezoelectric materials. Phys Chem Chem Phys. 2023;25:25925–25941.
933 28. Xu M, Wu S, Ding L, Lu C, Qian H, Qu J, Chen Y. Engineering ultrasound-activated piezoelectric
934 hydrogels with antibacterial activity to promote wound healing. J Mater Chem B. 2023;11:4318–4329.
935 29. Feng X, Ma L, Lei J, Ouyang Q, Zeng Y, Luo Y, Zhang X, Song Y, Li G, Tan L, Liu X, Yang C.
936 Piezo-Augmented Sonosensitizer with Strong Ultrasound-Propelling Ability for Efficient Treatment of
937 Osteomyelitis. ACS Nano. 2022;16:2546–2557.
938 30. Xu Y, Xu C, Xie M, Lei J, Ma L, Duan D, Tan L, Wu S, Yang C, Feng X. Ultrasound-activated
939 piezoelectric catalysis and neurogenic activity for effective therapy of MRSA-infected bone defects by
940 phase/defect-engineered barium strontium titanate. Small Methods. 2025;9:e2402174.

31. Song Q, Wang D, Li H, Wang Z, Sun S, Wang Z, Liu Y, Lin S, Li G, Zhang S, Zhang P. Dual-response of a multi-functional microsphere system to ultrasound and microenvironment for enhanced bone defect treatment. Bioact Mater. 2024;32:304–318.

32. Dwyer DJ, Belenky PA, Yang JH, MacDonald IC, Martell JD, Takahashi N, Chan CTY, Lobritz MA, Braff D, Schwarz EG, Ye JD, Pati M, Vercruysse M, Ralifo PS, Allison KR, Khalil AS, Ting AY, Walker GC, Collins JJ. Antibiotics induce redox-related physiological alterations as part of their lethality. Proc Natl Acad Sci U S A. 2014;111:E2100–E2109.

33. Lobritz MA, Belenky P, Porter CBM, Gutierrez A, Yang JH, Schwarz EG, Dwyer DJ, Khalil AS, Collins JJ. Antibiotic efficacy is linked to bacterial cellular respiration. Proc Natl Acad Sci U S A. 2015;112:8173–8180.

34. Karau MJ, Schmidt-Malan SM, Greenwood-Quaintance KE, Mandrekar J, Cai J, Pierce WM Jr, Merten K, Patel R. Treatment of methicillin-resistant *Staphylococcus aureus* experimental osteomyelitis with bone-targeted vancomycin. SpringerPlus. 2013;2:329.

35. Rastogi RP, Singh SP, Häder DP, Sinha RP. Detection of reactive oxygen species (ROS) by the oxidant-sensing probe 2′,7′-dichlorodihydrofluorescein diacetate in the cyanobacterium *Anabaena variabilis* PCC 7937. Biochem Biophys Res Commun. 2010;397:603–607.

36. Hirayama T, Niwa M, Hirosawa S, Nagasawa H. High-Throughput Screening for the Discovery of Iron Homeostasis Modulators Using an Extremely Sensitive Fluorescent Probe. ACS Sens. 2020;5:2950–2958.

37. Li D, Gromov K, Søballe K, Puzas JE, O'Keefe RJ, Awad H, Drissi H, Schwarz EM. Quantitative mouse model of implant-associated osteomyelitis and the kinetics of microbial growth, osteolysis, and humoral immunity. J Orthop Res. 2008;26:96–105.

Supplementary Files

This is a list of supplementary files associated with this preprint. Click to download.

- SupportingInformation.docx